

Effect of Rarefaction on Plume Expansion in Outer Space Conditions

Apurva Bhagat



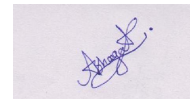
भारतीय प्रौद्योगिकी संस्थान हैदराबाद
Indian Institute of Technology Hyderabad

Department of Mechanical & Aerospace Engineering

19 June 2015

Declaration

I declare that this written submission represents my ideas in my own words, and where ideas or words of others have been included, I have adequately cited and referenced the original sources. I also declare that I have adhered to all principles of academic honesty and integrity and have not misrepresented or fabricated or falsified any idea/data/fact/source in my submission. I understand that any violation of the above will be a cause for disciplinary action by the Institute and can also evoke penal action from the sources that have thus not been properly cited, or from whom proper permission has not been taken when needed.



(Signature)

(Apurva Bhagat)

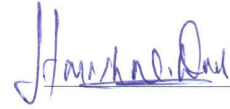
(ME13M1026)

Approval Sheet

This Thesis entitled Effect of Rarefaction on Plume Expansion in Outer Space Conditions by Apurva Bhagat is approved for the degree of Master of Technology from IIT Hyderabad



(Dr. B. S. Subhashchandra) Examiner
Associate Director
DRDL



(Dr. Harish Dixit) Examiner
Dept. of Mechanical & Aerospace Engineering
IITH



(Dr. Nishanth Dongari) Adviser
Dept. of Mechanical & Aerospace Engineering
IITH

Acknowledgements

I am grateful to my instructor Dr. Nishanth Dongari to allow me the freedom to work and at the same time to keep an eye to see that I do not get drifted from the main objective. His mentorship was paramount in providing a well rounded experience consistent my long-term career goals. His honesty and humility, has always motivated us to work harder and has kept us grounded. I am not sure many graduate students are given the opportunity to develop their own individuality and self-sufficiency by being allowed to work with such independence. And simultaneously, he has been the source of motivation for all our friends. Thus, the work environment, I have got to work has been vibrant and energetic.

I would like to thank my friends Ashwani Assam and Harshal Gijare for their valuable suggestions at various points of the thesis and for maintaining an atmosphere of co-operation and friendship. Thus, have made the thesis a joyful experience and journey.

I would like to thank Mechanical and Aerospace Department of IITH and the entire IIT Hyderabad system for providing us an excellent computational facility to work upon.

My highest gratitude goes to Dr.V.K.Saraswat, who came at the point in my academic career that has boosted my interest for working in the area of high-speed flow.

At last I would like thank my parents and family for their support, patience and faith in me and allowing me to be as ambitious as I wanted. It was under their watchful eye that I gained so much drive and an ability to tackle challenges head on.

Abstract

We carry out simulations to investigate the backflow analysis of plume expansion into rarefied atmosphere for a supersonic rocket model. The open source software OpenFOAM (Open Field Operation and Manipulation) is used with the compressible computational fluid dynamics (CFD) solver *rhoCentralFoam*. The flow fields are computed by the steady Reynolds-Averaged NavierStokes (RANS) solver with $k-\omega$ SST two equation turbulence model. Due to the existence of rarefaction conditions in outer-atmosphere, we have implemented the first-order Maxwell slip boundary condition for the velocity and Smoluchowski jump for the temperature. *rhoCentralFoam* solver has been validated with the experimental data for a nozzle flow in the slip flow regime. Major objective of the thesis is to study sensitivity of backflow w.r.t. degree of rarefaction and under different supersonic free-stream conditions. We report results of heat transfer and pressure coefficients for different free-stream Mach numbers at altitude conditions 80 km and 90 km. It is noticed that the slip results for heat transfer coefficient significantly differ from the no-slip ones.

Contents

Declaration	ii
Approval Sheet	iii
Acknowledgements	iv
Abstract	v
1 Introduction	7
1.1 Literature review	7
1.2 Objective of present work	9
2 Numerical Methodology	11
2.1 Governing equations	11
2.2 The <i>rhoCentralFoam</i>	12
2.2.1 Algorithm for <i>rhoCentralFoam</i>	12
2.2.2 Sutherland's viscosity model	13
2.2.3 Boundary conditions	13
2.2.4 Turbulence modelling	14
3 Validations	16
3.1 Conical nozzle	16
3.2 External Flow over a Supersonic Rocket	18
3.3 Rothe Nozzle	19
4 Test cases : Results and Discussion	23
4.0.1 Coefficient of Pressure	25
4.0.2 Coefficient of Heat Transfer	31
4.0.3 Coefficient of Drag	34
4.0.4 Normalized density	37
4.0.5 Axial and Radial slip velocity	38
4.0.6 Temperature Jump	39

4.0.7	Contours of different properties on the computational domain	40
5	Conclusion and Future work	44
	References	46

List of Tables

4.1	Average pressure coefficient values for different flow conditions (at 80 km and 90 km altitude, and free-stream Mach number 0, 2 and 4) and percentage deviation in between slip and no slip CFD for overall critical region.	30
4.2	Average pressure coefficient values for different flow conditions (at 80 km and 90 km altitude, and free-stream Mach number 0, 2 and 4) and percentage deviation in between slip and no slip CFD for critical zone 1.	30
4.3	Average pressure coefficient values for different flow conditions (at 80 km and 90 km altitude, and free-stream Mach number 0, 2 and 4) and percentage deviation in between slip and no slip CFD for critical zone 2.	30
4.4	Average heat transfer coefficient values for different flow conditions (at 80 km and 90 km altitude, and free-stream Mach number 0, 2 and 4) and percentage deviation in between slip and no slip CFD for overall critical region.	33
4.5	Average heat transfer coefficient values for different flow conditions (at 80 km and 90 km altitude, and free-stream Mach number 0, 2 and 4) and percentage deviation in between slip and no slip CFD for critical zone 1.	33
4.6	Average heat transfer coefficient values for different flow conditions (at 80 km and 90 km altitude, and free-stream Mach number 0, 2 and 4) and percentage deviation in between slip and no slip CFD for critical zone 2.	33
4.7	Average drag coefficient values for different flow conditions and percentage deviation in slip-no slip CFD throughout the critical wall	36
4.8	Average drag coefficient values for different flow conditions and percentage deviation in slip-no slip CFD (critical zone 1)	36
4.9	Average drag coefficient values for different flow conditions and percentage deviation in slip-no slip CFD (critical zone 2)	36

List of Figures

3.1	Mach number variation along the centreline of nozzle (<i>rhoCentralFoam</i> is validated against Fluent)	17
3.2	Contours of velocity magnitude in the nozzle flow. (<i>rhoCentralFoam</i> solver (b) is validated against Fluent (a))	17
3.3	Contours of temperature magnitude in the nozzle flow. (<i>rhoCentralFoam</i> solver (b) is validated against Fluent (a))	17
3.4	(a) Variation of pressure coefficient (C_p) on the surface of VLS central body [1] and (b) Mach number contours in the whole computational domain	18
3.5	Schematic of Rothe nozzle [2] (Dimensions are in mm)	19
3.6	(a) Centre line density variation in the nozzle, where $x = 0$ denotes the throat location and (b) density variation in the radial direction at 0.0477m. Both slip and no slip solutions of <i>rhoCentralFoam</i> are compared with experimental data [2].	21
3.7	(a) Centre line temperature variation in the nozzle, where $x = 0$ denotes the throat location and (b) temperature variation in the radial direction at 0.0477m. Both slip and no slip solutions of <i>rhoCentralFoam</i> are compared with experimental data [2].	21
3.8	Pressure contours inside the Rothe nozzle, (a) <i>rhoCentralFoam</i> with no-slip & no-jump boundary conditions, (b) <i>rhoCentralFoam</i> with first order slip and jump boundary conditions	22
3.9	Temperature contours inside the Rothe nozzle, (a) <i>rhoCentralFoam</i> with no-slip & no-jump boundary conditions, (b) <i>rhoCentralFoam</i> with first order slip and jump boundary conditions	22
3.10	Velocity contours inside the Rothe nozzle, (a) <i>rhoCentralFoam</i> with no-slip & no-jump boundary conditions, (b) <i>rhoCentralFoam</i> with first order slip and jump boundary conditions	22

4.1	Schematic of Sonda II rocket [1] (dimensions in meters)	23
4.2	Computational domain of the test case with unstructured mesh. The adaptive mesh is used based on the thermodynamic flow gradients. . .	24
4.3	Zoomed view of Sonda II rocket schematic at the tail. The indicated bold line is the critical region of interest in the current study on which arclength dimensions are denoted (dimensions in meters).	24
4.4	Variation of coefficient of pressure (C_p) along the arclength on critical zone 1 for 80 km (a, c and e) and 90 km (b, d, f) altitude conditions. Comparisons are made between slip CFD and no slip CFD results for free-stream Mach numbers 0 (fig a and b), 2 (fig c and d) and 4 (fig e and f).	27
4.5	Variation of coefficient of pressure (C_p) along the arclength on critical zone 2 for 80 km (a, c and e) and 90 km (b, d, f) altitude conditions. Comparisons are made between slip CFD and no slip CFD results for free-stream Mach numbers 0 (fig a and b), 2 (fig c and d) and 4 (fig e and f).	28
4.6	Variation of coefficient of pressure (C_p) along the arclength on critical zone 1 for (a) 80 km and (b) 90 km altitude respectively. Comparisons are made between three different Mach numbers (0, 2 and 4) for slip CFD cases.	29
4.7	Variation of coefficient of pressure (C_p) along the arclength on critical zone 2 for (a) 80 km and (b) 90 km altitude respectively. Comparisons are made between three different Mach numbers (0, 2 and 4) for slip CFD cases.	29
4.8	Variation of coefficient of pressure (C_h) along the arclength on critical zone 1 for (a) 80 km and (b) 90 km altitude respectively. Comparisons are made between three different Mach numbers (0, 2 and 4) for slip CFD cases.	32
4.9	Variation of coefficient of heat transfer (C_h) along the arclength on critical zone 2 for (a) 80 km and (b) 90 km altitude respectively. Comparisons are made between three different Mach numbers (0, 2 and 4) for slip CFD cases.	32
4.10	Variation of coefficient of drag (C_D) along the arclength on critical zone 1 for (a) 80 km and (b) 90 km altitude respectively. Comparisons are made between three different Mach numbers (0, 2 and 4) for slip CFD cases.	35

4.11	Variation of coefficient of drag (C_D) along the arclength on critical zone 2 for (a) 80 km and (b) 90 km altitude respectively. Comparisons are made between three different Mach numbers (0, 2 and 4) for slip CFD cases.	35
4.12	Variation of normalized density along the arclength on critical zone 1 (a) and critical zone 2 (b). Comparisons are made between 80 km and 90 km altitude conditions for quiescent atmosphere case.	37
4.13	Variation of normalized density along the arclength on the entire critical zone. Comparisons are made between different free-stream Mach numbers (0, 2 and 4) at 80 km (a) and 90 km (b) altitude conditions.	37
4.14	Variation of normalized axial slip velocity (a) and normalized radial slip velocity (b) along the arclength on the entire critical zone. Comparisons are made between 80 km and 90 km altitude conditions for quiescent atmosphere case.	38
4.15	Variation of normalized axial slip velocity along the arclength on the entire critical zone. Comparisons are made between different free-stream Mach numbers (0, 2 and 4) at 80 km (a) and 90 km (b) altitude conditions.	39
4.16	Variation of normalized radial slip velocity along the arclength on the entire critical zone. Comparisons are made between different free-stream Mach numbers (0, 2 and 4) at 80 km (a) and 90 km (b) altitude conditions.	39
4.17	Normalised temperature jump at 80km and 90km altitude	40
4.18	Variation of normalized temperature along the arclength on the entire critical zone. Comparisons are made between different free-stream Mach numbers (0, 2 and 4) at 80 km (a) and 90 km (b) altitude conditions.	40
4.19	Velocity contours of free-stream flow at Mach 2 without plumes at altitude 80km	40
4.20	Velocity contours at 80km altitude for quiescent atmosphere case (a), freestream Mach 2 case (c), freestream Mach 4 case (e). Velocity contours at 90km altitude for quiescent atmosphere case (b), freestream Mach 2 case (d), freestream Mach 4 case (f). Results of slip CFD are reported.	42

4.21 Temperature contours at 80km altitude for quiescent atmosphere case (a), freestream Mach 2 case (c), freestream Mach 4 case (e). Temperature contours at 90km altitude for quiescent atmosphere case (b), freestream Mach 2 case (d), freestream Mach 4 case (f). Results of slip CFD are reported. 43

List of Symbols

Nomenclature

C_h	heat transfer coefficient
C_p	pressure coefficient
C_D	drag coefficient
p	pressure
T	temperature
U	velocity
U_x	axial velocity
U_y	radial velocity
c_p	specific heat at constant pressure
H	specific enthalpy
k	thermal conductivity
R	gas constant
B	Reynolds number
Pr	Prandtl number
Kn	Knudsen number
Ma	Mach number

Greek letters

ρ	density
λ	mean free path
μ	dynamic viscosity
σ_v	tangential momentum accommodation coefficient
σ_T	thermal accommodation coefficient
γ	ratio of specific heats

Subscript

∞	freestream condition
f	fluid
w	wall
x	axial co-ordinate
y	normal co-ordinate
0	stagnation condition

Chapter 1

Introduction

1.1 Literature review

Supersonic under-expanded jet plumes in the rarefied atmosphere will lead to back flow phenomena [3]. This back flow effect causes unanticipated aero-thermodynamics effects like enhancement of heat load, excessive contamination from plume gases and erosion of critical surfaces [4]. In addition, back flow of plume will also interact with the supersonic free-stream flow leading to cause more severe effects on the critical surfaces. Therefore an accurate prediction of aero-thermodynamic loads due to plume expansion and interaction on critical parts is necessary for aerospace applications.

Early investigations on underexpanded exhaust plumes consist of experiments supplemented by method of characteristics and shock expansion techniques [5, 6]. The overall structure of highly underexpanded jets in quiescent atmosphere is investigated by Love [5], Adamson and Nicholls [7] and Latvala [8]. It is determined that the dimensions of exhaust plumes in quiescent atmosphere scale as the inverse square root of the ambient pressure. Woronowicz *et al.* [9] derived an analytical solution for one-dimensional unsteady free jet expansion in to a vacuum. The widely used cosine law or the Boynton/Simons plume model [10, 11] provides an approximate farfield density distribution which takes a form of a cosine function. Based on these, Cai *et al.* [12] presented a set of gaskinetic solutions to the problem of unsteady collisionless round plume development. Manski *et al.* [13] presented the analytical results of large H_2/O_2 rocket nozzles and performed various calculations of rocket nozzles by changing rocket design parameters vs thrust, chamber pressure, mixture ratio, nozzle area ratio and nozzle geometry.

There has been significant progress in the numerical modeling of rocket plumes in recent years using the computational fluid dynamics (CFD) techniques. Bakker *et*

al. [14] investigated base flow plume interaction at moderate nozzle pressure ratios, the influence of numerical discretization technique and turbulence models on the final results. They have also studied the influence of boat-tailing in presence of an exhaust jet and underexpanding cases at higher altitudes. Buanga *et al.* [15] investigated the base-flow of a generic blunt rocket configuration for two different complex model configurations under subsonic and hypersonic flow conditions using Reynolds-averaged NavierStokes (RANS) based DLR TAU code. Viti *et al.* [16] carried out numerical simulations of a sonic circular jet exhausting into a turbulent supersonic cross flow using 3 dimensional RANS based code. They investigated that the trailing vortices are the main mechanism responsible for the mixing of the injectant with the freestream fluid. Rana *et al.* [17] performed classical large eddy simulations for sonic jet issued in a Mach 1.6 freestream cross-flow and demonstrated the averaged and instantaneous flow features including vortex structures downstream of the jet injection, along with the jet penetration, jet mixing, pressure distributions, turbulent kinetic energy and Reynolds stresses in the downstream flow.

Several numerical simulations with the direct simulation Monte Carlo (DSMC) method have been carried out to validate analytical results. Burt *et al.* [18] proposed a simulation scheme for flow-field and radiation analysis of solid rocket exhaust plumes at high altitude. Gimelshein *et al.* [19] carried out DSMC simulations to investigate the interaction of a jet from a 3000-N-class thruster positioned on the side of small rocket with a rarified atmosphere at 80 km and 100 km. Chemical reactions between freestream and plumes have been included. The results presented for the flow field and surface mass flux demonstrated possible contamination of an onboard radiance sensor located on the cylindrical part of the rocket for different freestream and plume conditions.

The combination of Navier-Stokes solvers with DSMC seems to be the most popular, as mature implementations of both methods are available. Hybrid computations relevant to plume expansion and impingement have been carried out by Lumpkin *et al.* [20]. Missile flowfields with plumes and divert jets under high altitude conditions have been computed using coupled code of continuume CFD and DSMC by Papp *et al.* [21]. Numerical simulations and experimental works on vacuum plume and its effects have been reported by He *et al.* [22]. They carried out experiments in a supersonic low density wind tunnel and simulated the same using DSMC and Naviers stoke combined approach to verify PWS (Plume workstation) software. Results of numerical study of continuum jet interaction with a rarefied flow have been reported by Glass *et al.* [3] by developing three-dimensional uncoupled CFD-DSMC

code. Gimelshein *et al.* [23] examined a two-phase plume flow from a small aluminized propellant side thruster interacting with rarefied atmosphere at 120 km altitude numerically using a three step continuum-kinetic (hybrid) approach. The importance of two way coupling, particle radiative cooling, and molecule accommodation on particle surface have been analyzed. Vashchenkov *et al.* [24] have used hybrid approach to study of the mechanisms of the flow turn around the nozzle lip and the backflow origination. They investigated that the effects of viscosity become more significant with the flow expansion and dominate in the rarefied regime.

In the literature, various researchers have proposed many CFD, DSMC and hybrid approaches to investigate plume expansion and interaction problems. CFD methods are only valid in the continuum regime, i. e. altitude less than 40km. While DSMC simulations are computationally intensive as these class of problems involve the continuum plume jet at the exit of the nozzle and indeed not so feasible for 3-D geometries. On the other hand, the switching criterion for hybrid methods are not yet generalised enough to apply in practical scenarios. Alternatively, few researchers have been exploring extended hydrodynamic methods, such as applying non-equilibrium boundary conditions (BCs) at the wall surfaces [ref] and/or employing non-linear/higher-order constitutive relations [ref] . The major objective of this thesis is to obtain accurate flow data for calculating realistic thermal load predictions from highly under-expanded plumes in continuum-transition regime using extended CFD i.e. open source CFD tool OpenFOAM which is parallel friendly implemented with the first order Maxwellian velocity slip and Smoluchowski temperature jump.

In this thesis, we have analysed plumes expanding in quiescent atmosphere as well as supersonic free-stream flow conditions at 80km and 90km altitude. Aerothermodynamic parameters like heat transfer, pressure and friction coefficients on the critical areas of rocket configuration are reported. Major objective is to study effect of degree of rarefaction on these parameters by comparing CFD and extended CFD results.

1.2 Objective of present work

- To validate the *rhoCentralFoam* solver using first-order Maxwell's velocity slip and the Smoluchowski temperature jump boundary conditions for different test cases with experimental data.
- To present the results of simulations carried out to measure temperature jump,

velocity slip, heat load and drag forces on the critical wall prone to plume impingement. Other thermodynamic parameters of interest are also briefly presented. Test cases cover free-stream Mach number 0, 2, 4 and at two different altitudes of 80 and 90 km.

- The major objective has been to investigate the influence of rarefaction on the drag, pressure and heat transfer coefficients by comparing the conventional CFD using no-slip boundary condition with slip CFD results.

Chapter 2

Numerical Methodology

2.1 Governing equations

We solve the governing equations of fluid motion for the Eulerian phase. These equations are discretised and subsequently solved using the Finite-Volume method. The equations are expressed as a set of partial differential equations (PDEs) which are derived by the application of the laws of conservation to fluid motion.

Conservation of mass (Continuity equation):

$$\frac{\partial \rho}{\partial t} + \nabla \cdot [\vec{u} \rho] = 0 \quad (2.1)$$

Conservation of momentum neglecting gravity and particle drag:

$$\frac{\partial(\rho \vec{u})}{\partial t} + \nabla \cdot [\vec{u}(\rho \vec{u})] + \nabla p + \nabla \cdot \sigma = 0 \quad (2.2)$$

where σ is the viscous stress tensor considered positive in compression.

Conservation of energy:

$$\frac{\partial(\rho E)}{\partial t} + \nabla \cdot [\vec{u}(\rho E)] + \nabla \cdot (\vec{u} p) + \nabla \cdot (\sigma \cdot \vec{u}) = \nabla \cdot (k \nabla T) \quad (2.3)$$

where, the primary variable (ρE) is total energy of the system, k is thermal conductivity and T is temperature and $E = e + \frac{|u^2|}{2}$, where $e = c_v T = (\gamma - 1)RT$ is the specific internal energy and $\gamma = \frac{c_p}{c_v}$ is the ratio of specific heats at constant pressure and volume.

The value of temperature is calculated as:

$$T = \frac{1}{c_v} \left(\frac{\rho E}{\rho} - \frac{|u^2|}{2} \right) \quad (2.4)$$

The above four equations are closed by the ideal gas equation of state:

$$p = \rho RT \quad (2.5)$$

2.2 The *rhoCentralFoam*

The *rhoCentralFoam* is density-based compressible flow solver based on central upwind schemes of Kurganov and Tadmor [25, 26].

The *rhoCentralFoam* solver has been validated by Greenshields *et al.* [27] for supersonic jet experiment by Ladenburg *et al.* [28] and various standard compressible flow cases. Bansal *et al.* [29] have used this solver to simulate the hypersonic flow around an entry vehicle in the Martian atmosphere. Nakao *et al.* [30] have validated this solver against cryogenic wind tunnel data for sub-sonic flow around a NACA airfoil. This solver have also been validated for supersonic compressible flow around circular cylinders [31] and backward-facing step [32].

2.2.1 Algorithm for *rhoCentralFoam*

The viscous momentum and energy equations are solved using the time-splitting approach. In this approach, the inviscid equations are solved explicitly, by the ‘fvc::’ operator, to obtain a predicted value of the variable. Later, the diffusion terms are then introduced as implicit corrections to the original inviscid equations, represented by the ‘fvm::’ operator.

The solution starts with the calculation of $\rho_{f\pm}$, $T_{f\pm}$ and $u_{f\pm}$ at the face of the cell, split into outgoing and incoming directions. The face values are interpolated from the values at the cell centers and substituted in the calculation of the convective fluxes. Thereafter continuity equation is solved to obtain density, ρ . The predicted value of the velocity, (\tilde{u}) is calculated explicitly from the inviscid momentum equation:

$$\frac{(\rho\tilde{u}) - (\rho u^n)}{\partial t} + \nabla \cdot [u(\rho u)] + \nabla p = 0 \quad (2.6)$$

$$\tilde{u} = \frac{(\rho\tilde{u})}{\rho} \quad (2.7)$$

The value of \tilde{u} is then used to calculate the corrected value of velocity at the next time step (denoted as n+1) implicitly, from the viscous momentum Equation.

$$\frac{(\rho u)^{n+1} - (\tilde{\rho} \tilde{u})}{\partial t} - \nabla \cdot (\mu \nabla u) = 0 \quad (2.8)$$

The energy equation is solved in the similar manner. A predictor value of the energy flux ($\tilde{\rho} \tilde{E}$) is first calculated from the inviscid energy equation.

$$\frac{\partial(\rho E)}{\partial t} + \nabla \cdot [u(E + p)] + \nabla \cdot (\sigma \cdot u) = 0 \quad (2.9)$$

The temperature, T is obtained using Equation 2.4, which takes ρ , u and E as input. The estimated value of T is then used in the corrected energy equation:

$$\frac{\partial(\rho c_v T)}{\partial t} - \nabla \cdot (k \nabla T) = 0 \quad (2.10)$$

The pressure is then updated using the ideal gas equation of state (Equation 2.5).

2.2.2 Sutherland's viscosity model

Sutherland's law of viscosity is used to model the viscosity μ :

$$\mu = \mu_{ref} \frac{T^{1.5}}{T + T_{ref}} \quad (2.11)$$

T = 110.4 K is the reference temperature. $\mu_{ref} = 1 : 716 \times 10^{-5} \frac{N \cdot s}{m^2}$ is the reference viscosity.

2.2.3 Boundary conditions

The continuum regime of gas flows are simulated by solving the Navier-Stokes-Fourier (N-S-F) equations along with the no-slip boundary condition for velocity and no jump for temperature. However, experiments such as those performed by Arkilic [33] and Colin [34] have shown that the conventional N-S-F equations may not produce accurate results for rarefied gas flows. It is normal practice to determine the rarefaction degree of gas flows by the Knudsen number (Kn). The N-S-F equations applied with continuous boundary conditions of velocity and temperature are commonly known to be valid up to a Knudsen number of 0.001 if no discontinuous boundary conditions are applied [35]. However, the applicability of the N-S-F equations can be extended to

$Kn \sim 0.1$ if non-equilibrium boundary conditions of velocity slip and temperature jump are applied [36]. A kinetic approach is ideally necessary in order to simulate gas flows with Kn numbers higher than 0.1, for example, the direct simulation Monte Carlo (DSMC).

Maxwellian velocity slip is defined as

$$U_f - U_w = \frac{2 - \sigma_v}{\sigma_v} \lambda \frac{\partial u}{\partial y} + \frac{3}{4} \frac{\mu}{\rho T} \frac{\partial T}{\partial x}, \quad (2.12)$$

where U_f is the fluid velocity, U_w is the reference wall velocity, λ is the mean free path of gas, μ is dynamic viscosity, ρ is density of fluid, x is the axial co-ordinate, y is the normal co-ordinate, σ_v is tangential momentum accommodation coefficient and T is temperature.

Smoluchowski Temperature Jump is defined as

$$T_f - T_w = \frac{2 - \sigma_T}{\sigma_T} \frac{2\gamma}{\gamma + 1} \frac{\lambda}{Pr} \frac{\partial T}{\partial y}, \quad (2.13)$$

and

$$Pr = \frac{\mu c_p}{k}, \quad (2.14)$$

where T_f is the temperature of fluid, T_w is the reference wall temperature, Pr is the non-dimensional Prandtl number, σ_T is thermal accommodation coefficient, γ is specific heat ratio, c_p is specific heat and k is thermal conductivity.

The *rhoCentralFoam* using the conventional boundary conditions is referred as **no slip**, and with the slip boundary condition is referred as **slip** throughout in this thesis.

2.2.4 Turbulence modelling

We have used the $k-\omega$ SST turbulence model as it gives very good results at turbulent mixing layer region and it is believed that the base flow characteristics cannot be predicted accurately by eddy-viscosity turbulence models [37]. $k-\omega$ SST turbulence model is implemented which is the mix of $k-\omega$ and $k-\epsilon$ models. The *rhoCentralFoam* solver with $k-\omega$ SST turbulence model has been validated with analytical results for an electrospray RF ion Funnel [38] and with experimental data for transonic turbulent flow over a deep cavity [39]. In the near-wall region the $k-\omega$ model is used and further away from the wall in the fully turbulent regions the $k-\epsilon$ method

is used. The $k - \omega$ *SST* model is merited for its good behaviour in adverse pressure gradients and separating flow [40, 41]. The shear stress transport (SST) formulation combines the best of two methods. Blending functions are implemented to assure a smooth transition between the $k - \omega$ model and the $k - \epsilon$ model [42].

Chapter 3

Validations

3.1 Conical nozzle

A supersonic rocket engine nozzle geometry [43] is considered for the validation of the *rhoCentralFoam* solver against commercial CFD tool Fluent. Half convergent angle of nozzle is 30° and half divergent angle is 4° . Inlet, throat and exit width of nozzle are 1 m, 0.304 m and 0.861 m respectively. Computational domain is a 2 dimensional half nozzle configuration which is considered symmetric about axis. Mesh has been created with ICEM CFD tool which is structured and consists 14500 cells. Same mesh is used to obtain results using compressible solver Fluent and *rhoCentralFoam* solver of OpenFOAM. Stagnation pressure at inlet is 44 bar and stagnation temperature is 3400 K. In both the solvers, we have neglected viscous effects.

Figure 3.1 shows the variation of Mach number along the centreline of nozzle. The *rhoCentralFoam* results find an excellent agreement with the Fluent one. Figures 3.2 and 3.3 demonstrate contours of velocity and temperature respectively and *rhoCentralFoam* is compared with Fluent. As pressure at the exit of the nozzle is less than the ambient pressure, shocks are produced inside the nozzle and hence it is an over-expanded supersonic nozzle. One oblique shock occurs just downstream of the throat of nozzle and other in the diverging part of nozzle. One can notice from Figs 3.2 and 3.3 that both, the *rhoCentralFoam* and Fluent predict identical phenomena.

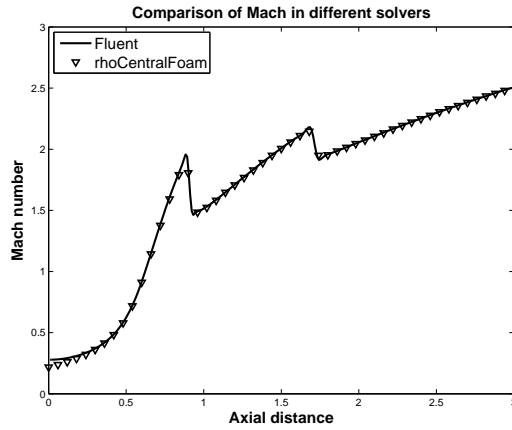


Figure 3.1: Mach number variation along the centreline of nozzle (*rhoCentralFoam* is validated against Fluent)

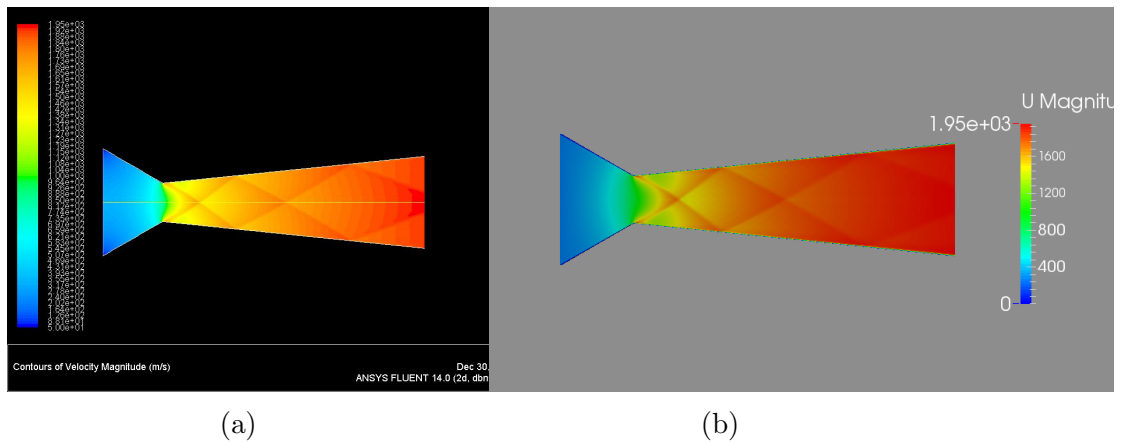


Figure 3.2: Contours of velocity magnitude in the nozzle flow. (*rhoCentralFoam* solver (b) is validated against Fluent (a))

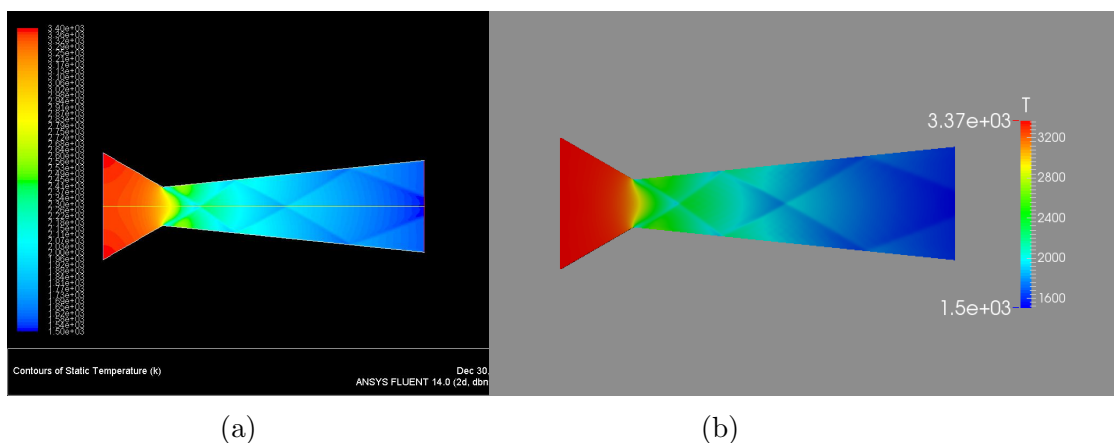


Figure 3.3: Contours of temperature magnitude in the nozzle flow. (*rhoCentralFoam* solver (b) is validated against Fluent (a))

3.2 External Flow over a Supersonic Rocket

The *rhoCentralFoam* solver is validated here for external flow over a supersonic rocket configuration, for pressure coefficient data available from wind tunnel experiments [1]. The data is available on VLS vehicle central body which is originally a four-stage satellite launcher built with four booster attached to a main body. Simulations are carried out for the flow over the VLS second stage flight configuration with freestream Mach number of 1.25 and angle of attack with 0° . Free-stream pressure and temperature conditions used corresponds to altitude of 5 km, which falls in the continuum flow regime. Therefore no slip and no jump boundary conditions are used on the wall.

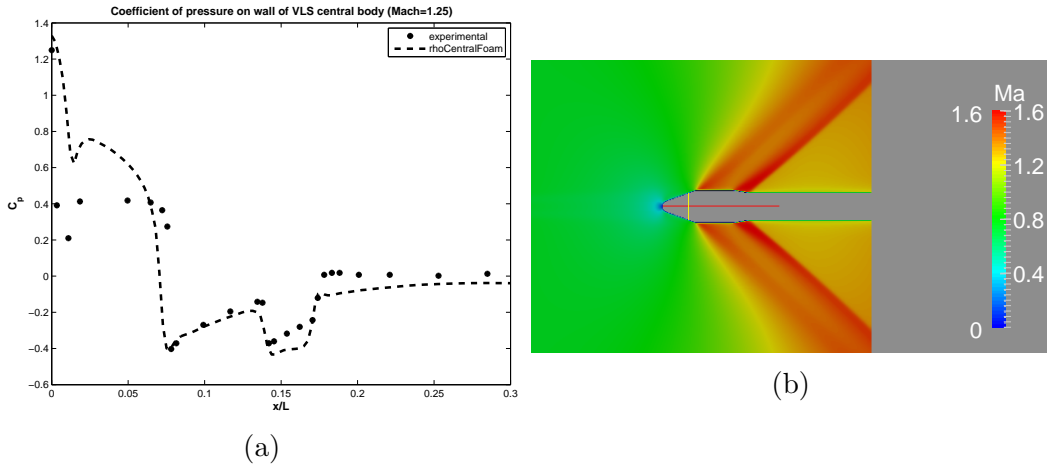


Figure 3.4: (a) Variation of pressure coefficient (C_p) on the surface of VLS central body [1] and (b) Mach number contours in the whole computational domain

Figure 3.4a shows C_p trends of experimental data and *rhoCentralFoam* results qualitatively compare each other very well. Deviation in results may be due to the approximated geometry. Minimum velocity is observed at stagnation point or nose of the rocket. Pressure coefficient drops at arlength 0.08m due to oblique shockwave and again drops slightly at 0.15 m due to secondary weak oblique shock wave.

3.3 Rothe Nozzle

The third case that we have chosen to validate the *rhoCentralFoam* solver is Rothe nozzle [2]. Here, experiments are carried out to measure density and temperature data along the centre-line and radially at few critical locations. Figure 3.5 demonstrates the schematic of Rothe nozzle. The inlet radius of the converging cone has a height of 8.3 mm and a half angle of 30 degrees. This is followed by a diverging cone with an exit radius of about 21 mm and a half angle of 20 degrees. The two cones are connected via a throat section with a radius 2.55 mm. The longitudinal radius of curvature at the throat is equivalent to half of the throat radius. The computational domain consists of an axisymmetric two degree wedge of the real nozzle. Although the nozzle geometry is given by Rothe [2], it is important to apply inlet and outlet domains to include certain upstream and downstream effects of the nozzle domain [44]. Upstream of the converging cone, a 5 mm long inlet domain is introduced. Downstream of the diverging cone is a vacuum chamber that is applied with a height of about 29 mm and a length of about 25 mm. For this nozzle, an air flow is present at the inlet and a vacuum condition at the outlet. The Reynolds number notation by Rothe [2], $B = \rho_0(2H_0)^{1/2}r/\mu_0$, is adopted in this investigation, where H_0 is the specific enthalpy, μ_0 is the dynamic viscosity, ρ_0 is density in the stagnation chamber and r is the throat radius. In this thesis, the $B = 590$ case of Rothe is chosen to be simulated, with an applied inlet pressure of 473.86 Pa and a temperature of 300 K [45]. The mesh of this test case is structured and consists of 24300 cells, where only one cell layer is placed in the symmetry direction. The side planes of the wedge are simulated as symmetry-planes by applying specular reflecting surfaces.

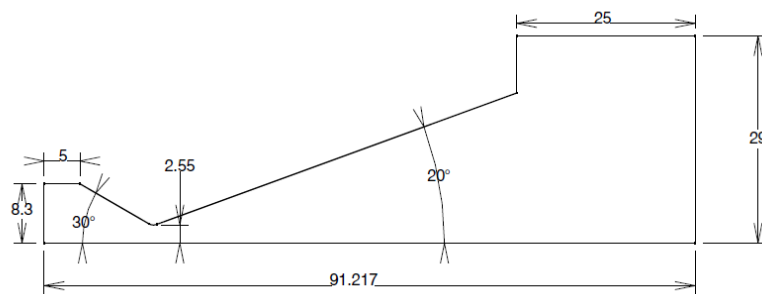


Figure 3.5: Schematic of Rothe nozzle [2] (Dimensions are in mm)

Here, the *rhoCentralFoam* solver is implemented with both the no slip and slip boundary conditions and experimental data [2] for temperature and density variations along the centreline of nozzle and along radial direction.

In the figure 3.6a, the centerline profile of mass density is displayed. It can be seen that slightly downstream from the throat, the *rhoCentralFoam* solver with slip and jump boundary conditions deviates slightly from the experimental data. Downstream of the throat both the solvers are considered to produce reasonable results. In the figure 3.6b, the radial profile of the density is displayed scaled by the axial value. It can be seen that the results of the *rhoCentralFoam* with slip and jump boundary conditions agree well with the experimental data.

In the figure 3.7a, the centerline profile of temperature is displayed. It can be seen that both the solvers produce reasonable results till an axial position of about 0.03 m after which slip CFD has significantly lower temperature than the experimental data. In the figure 3.7b, the radial profile of the temperature is displayed. Here it can be seen that results of *rhoCentralFoam* solver with no slip boundary conditions are scattered from the experimental data. However the *rhoCentralFoam* with slip boundary conditions manages to capture the validation temperature at the wall.

It can also be seen in figure 3.9, *rhoCentralFoam* with no slip BC is predicting higher temperature at wall as compared with slip BC. As nozzle exit conditions are equivalent to vaccume, free expansion of plumes is occuring at the nozzle exit (refer figure 3.8). The contours of other properties are shown in figures below. Figure 3.9 demonstrates contours of temperature within nozzle with slip and no slip CFD. As explained earlier, high temperature zone is observed near wall in no slip CFD whereas a clear temperature jump occurs on wall in slip CFD. As slip boundary conditions work well with rarified atmosphere, flow expands better and rapidly (higher velocity) with reduced temperature and pressure near nozzle exit with slip CFD.

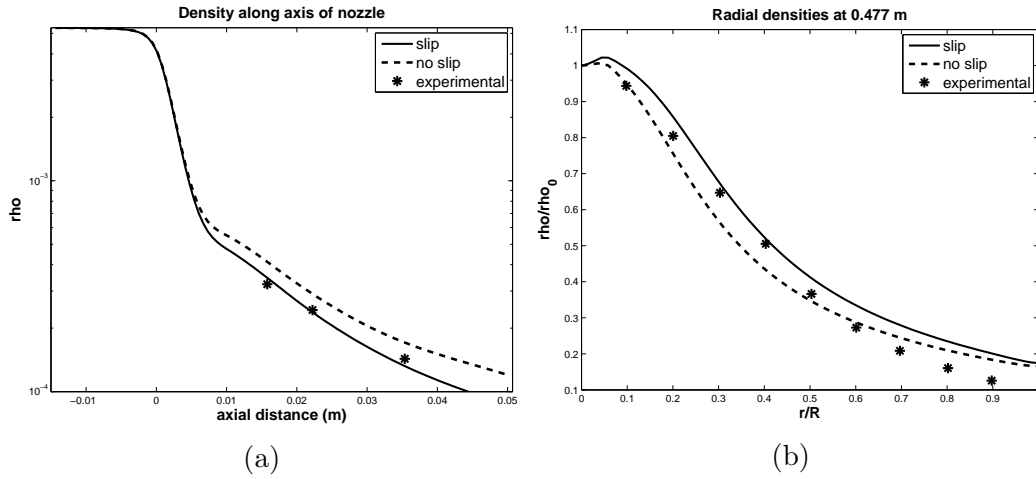


Figure 3.6: (a) Centre line density variation in the nozzle, where $x = 0$ denotes the throat location and (b) density variation in the radial direction at 0.0477m. Both slip and no slip solutions of *rhoCentralFoam* are compared with experimental data [2].

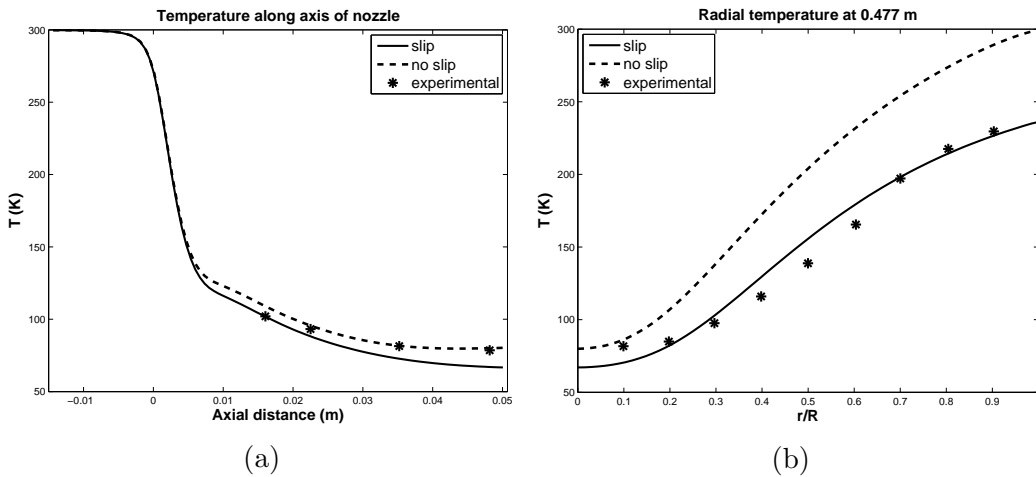


Figure 3.7: (a) Centre line temperature variation in the nozzle, where $x = 0$ denotes the throat location and (b) temperature variation in the radial direction at 0.0477m. Both slip and no slip solutions of *rhoCentralFoam* are compared with experimental data [2].

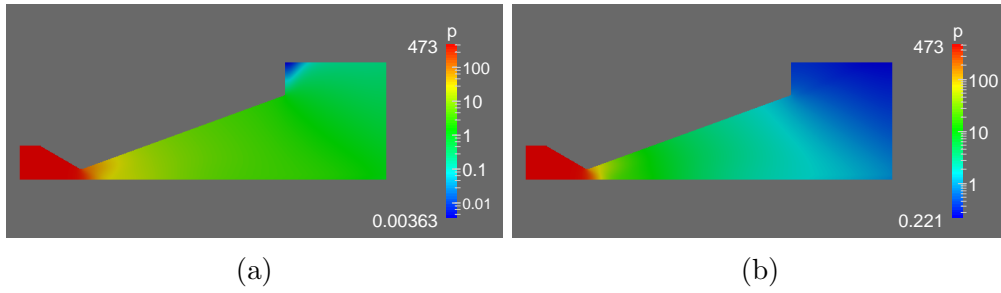


Figure 3.8: Pressure contours inside the Rothe nozzle, (a) *rhoCentralFoam* with no-slip & no-jump boundary conditions, (b) *rhoCentralFoam* with first order slip and jump boundary conditions

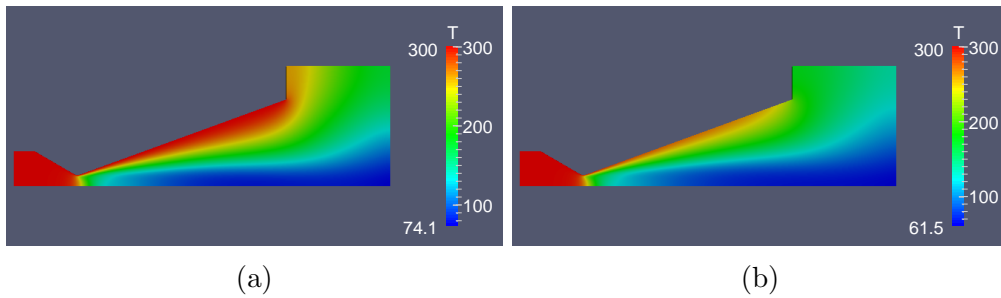


Figure 3.9: Temperature contours inside the Rothe nozzle, (a) *rhoCentralFoam* with no-slip & no-jump boundary conditions, (b) *rhoCentralFoam* with first order slip and jump boundary conditions

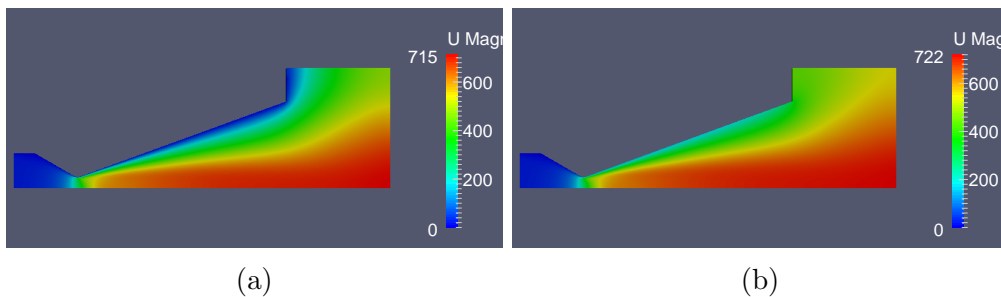


Figure 3.10: Velocity contours inside the Rothe nozzle, (a) *rhoCentralFoam* with no-slip & no-jump boundary conditions, (b) *rhoCentralFoam* with first order slip and jump boundary conditions

Chapter 4

Test cases : Results and Discussion

The *rhoCentralFoam* solver has been validated for the supersonic nozzle flow with plume expansion and supersonic flow past a model rocket configuration. The objective of the current thesis is to investigate the nozzle flow plume interaction with a supersonic free-stream and the backflow effect in the rarified atmosphere. We chose the test case with Sonda II rocket model configuration [1] for external body, while the nozzle configuration is similar to Rothe [2] with a geometrical scale up of 4.75 times in all dimensions. The schematic of the test case is given in Figure 4.1.



Figure 4.1: Schematic of Sonda II rocket [1] (dimensions in meters)

Sonda is a family of Brazilian-built sounding rockets which serves as a path to the VLS orbital rocket. It has a maximum flight altitude of 180 km which has been launched 7 times.

Figure 4.2 demonstrates the computational domain used for simulations which is adaptively tested for normalised density gradients. The mesh is unstructured of quad elements and has 27000 cells.

Underexpanded plumes will expand freely and impinge back onto the walls of rocket adjacent to nozzle. Investigation is carried out on critical parts which are prone to backflow and indeed where plume interaction takes place with a supersonic

free-stream. Critical region under study is demonstrated in figure 4.3 which is divided into two parts - critical zone 1 and critical zone 2. Critical zone 1 is where supersonic free-stream flow and plumes interact, while critical zone 2 is more prone to backflow of plume coming out of the nozzle. Arc-length varies along the arrow from 0 to 0.748 for critical zone 1 and from 0.748 to 1.231 for critical zone 2.

We have carried out the parametric study for the two dimensional geometry of Sonda II model configuration (shown in figures 4.1 and 4.2). Parameters include altitude variation of 80 km and 90 km, and free-stream Mach numbers of 0, 2 and 4. As plume expansion and free-stream interaction is a transient problem, we report all the results at time, $t = 0.025$ seconds.

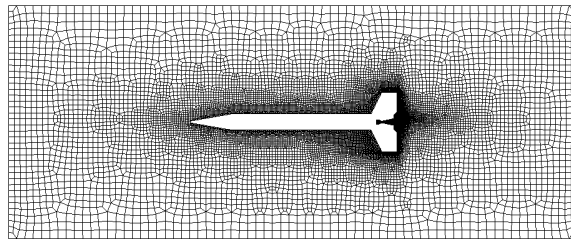


Figure 4.2: Computational domain of the test case with unstructured mesh. The adaptive mesh is used based on the thermodynamic flow gradients.

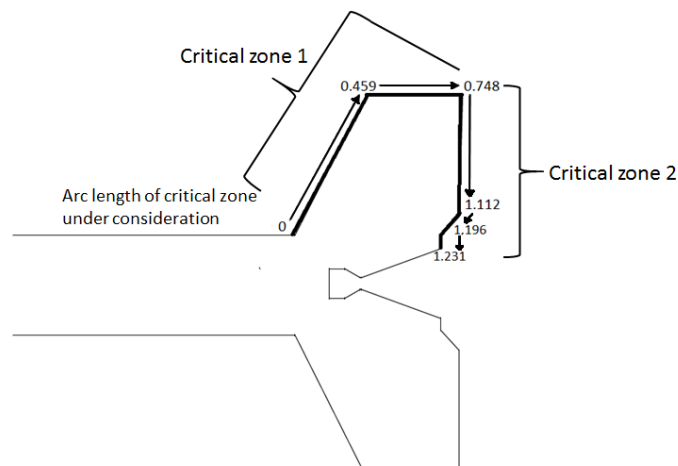


Figure 4.3: Zoomed view of Sonda II rocket schematic at the tail. The indicated bold line is the critical region of interest in the current study on which arclength dimensions are denoted (dimensions in meters).

4.0.1 Coefficient of Pressure

The pressure coefficient C_p shows the dynamic relative pressure on the critical wall, which is defined as follows

$$C_p = \frac{p_w - p_\infty}{\frac{1}{2}\rho_\infty U_\infty^2}, \quad (4.1)$$

where p_w is the static pressure on the critical wall. ρ_∞ and U_∞ are freestream density and velocity respectively. U_∞ is calculated from chamber conditions. We define it as

$$U_\infty = \sqrt{\gamma RT_0}, \quad (4.2)$$

where γ and R are specific heat ratio and gas constant for air respectively. And T_0 is the stagnation temperature in nozzle chamber which is 1000 K. One has to note that U_∞ is constant for all the test cases we have presented, as the chamber stagnation temperature remains constant.

Figures 4.4 and 4.5 demonstrate the pressure coefficient plotted along the arc-length on the critical zone 1 and 2, respectively. In all the cases C_p results with slip CFD and no slip CFD are almost overlapping on each other. Table 4.1 states that percentage deviation in slip and no slip results within 80 km and 90 km altitude is within 2 - 8 %. It shows that C_p is least sensitive to the altitude variation and remains unaffected with the degree of rarefaction in slip flow regime. Significantly large percentage deviation in slip and no slip values is observed at 90 km quiscent atmosphere case.

Figures 4.6 and 4.7 demonstrate the variation of coefficient of pressure (C_p) along the arclength on the critical zones 1 and 2, respectively. Comparisons are made between different Mach numbers (0, 2 and 4) for slip CFD cases. Here, plots (a) and (b) in both figures demonstrate 80 and 90 km respectively.

On critical zone 1, i.e. figure 4.6, as expected C_p value is close to zero for $Ma = 0$ case. For $Ma = 2$ case, it remains constant along the arc-length and a weak shock wave is noticed around the corner of wing (arclength = 0.459 m). However, for $Ma = 4$ case, the strength of the shock wave is significant and contrasting results are reported between 80 and 90 km. Between arc-length 0.457 to 0.75, the C_p value is increasing for 80 km condition, while there is sudden rise at 0.457 m and approximately constant on the later region, for 90 km one. This is because, oblique shocks at corner of the wings are stronger at 90 km and diffused at 80 km conditions. Rarefaction at 90 km leads to steep pressure gradients and strong shocks.

For all the cases, we can see a strong barrel shock wave occurring at 1.15 m that is located slightly after nozzle lip (see figure 4.5). Barrel shock which is a typical

characteristic of under-expanded jets is the line of demarcation between interior region and outer region, where the former is independent of ambient pressure and the later is influenced by the ambient pressure [46]. It can be seen that barrel shock, which is present at 1.15 m of arclength, is stronger in quiescent atmosphere (Mach = 0 case) as compared to that in supersonic free-stream flow conditions (refer figure 4.7a). This can be explained by the fact, that the external flow hits the expanding plume jet from nozzle and thus the freestream effectively changes its direction away from the nozzle axis. This also forms impingement shock wave and consequently pressure at the jet boundary increases. Expansion of plumes into the ambience is significantly reduced with increase in Mach number. Hence, the plume jet boundary turns towards the nozzle axis with increase in Ma , which causes the free-stream to expand i.e. drop in the pressure below initial ambient conditions. Both processes help to adjust the jet pressure to the ambient pressure and tend to dampen the formation of downstream shock cells, which are evidently present in the flowfield of under-expanded jets. The mechanism of adjusting jet pressure to ambient pressure is called the “supersonic pressure relief effect” [46]. This effect can be observed in figure 4.7a where barrel shock have been weakened as free-stream Mach number increases.

Barrel shock waves are relatively stronger at 90 km than at 80 km conditions as atmosphere is more rarefied at 90 km than at 80 km. Ambient pressure is 0.182 Pa at 90 km and therefore it is difficult for the jet pressure to adjust to low ambient pressure. Hence C_p is not much sensitive to free-stream Mach number at 90 km (see figure 4.7b).

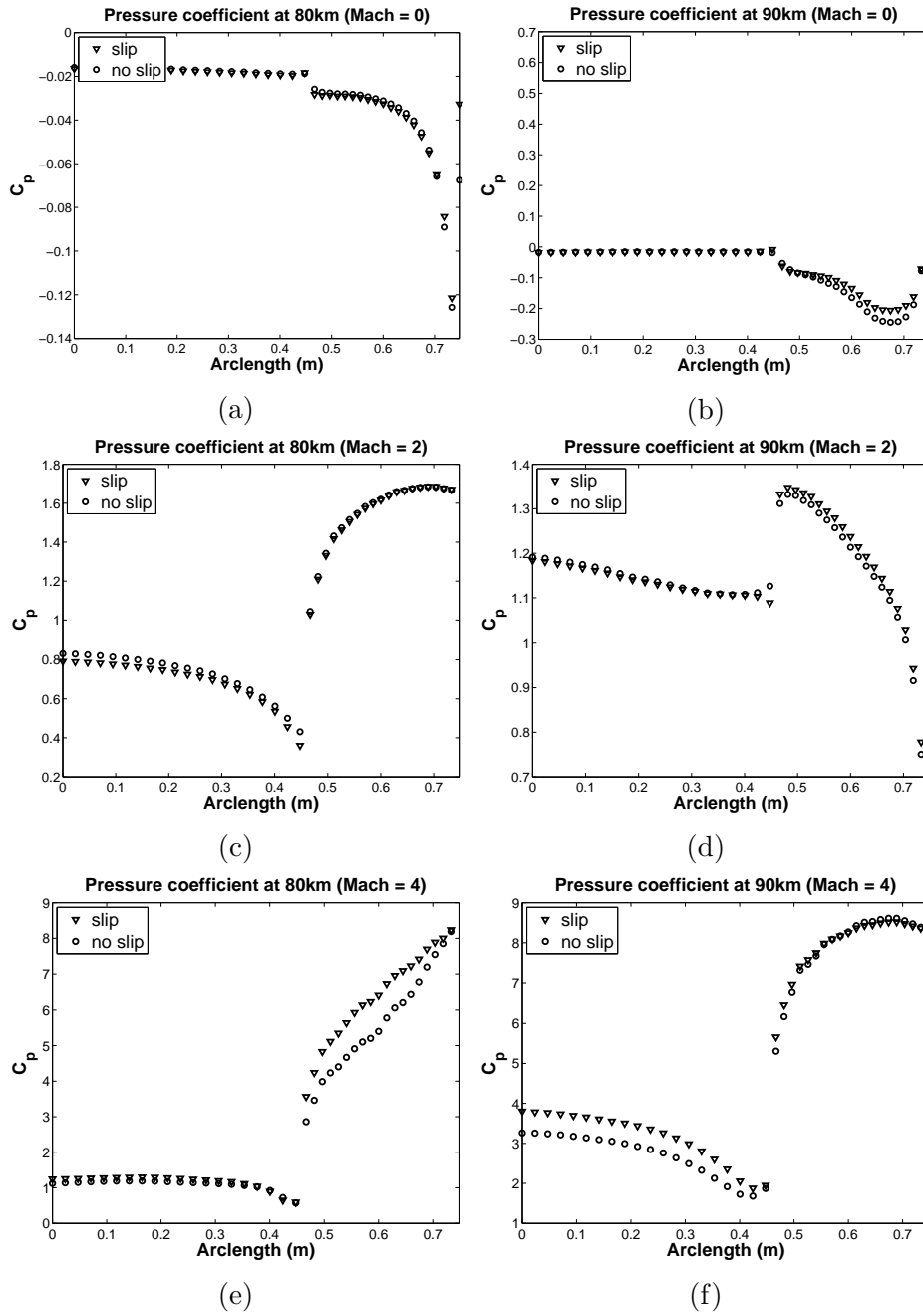


Figure 4.4: Variation of coefficient of pressure (C_p) along the arclength on critical zone 1 for 80 km (a, c and e) and 90 km (b, d, f) altitude conditions. Comparisons are made between slip CFD and no slip CFD results for free-stream Mach numbers 0 (fig a and b), 2 (fig c and d) and 4 (fig e and f).

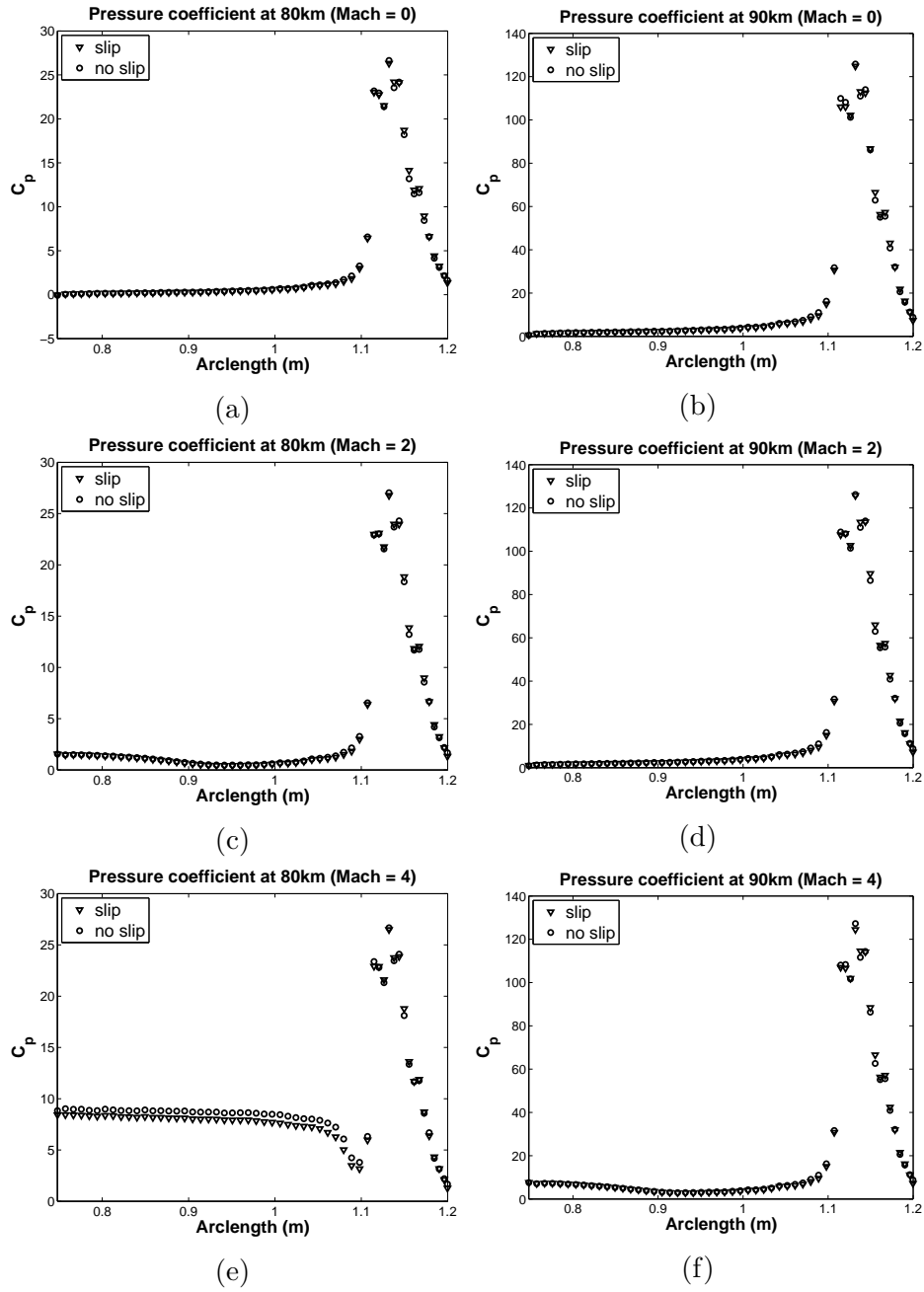


Figure 4.5: Variation of coefficient of pressure (C_p) along the arclength on critical zone 2 for 80 km (a, c and e) and 90 km (b, d, f) altitude conditions. Comparisons are made between slip CFD and no slip CFD results for free-stream Mach numbers 0 (fig a and b), 2 (fig c and d) and 4 (fig e and f).

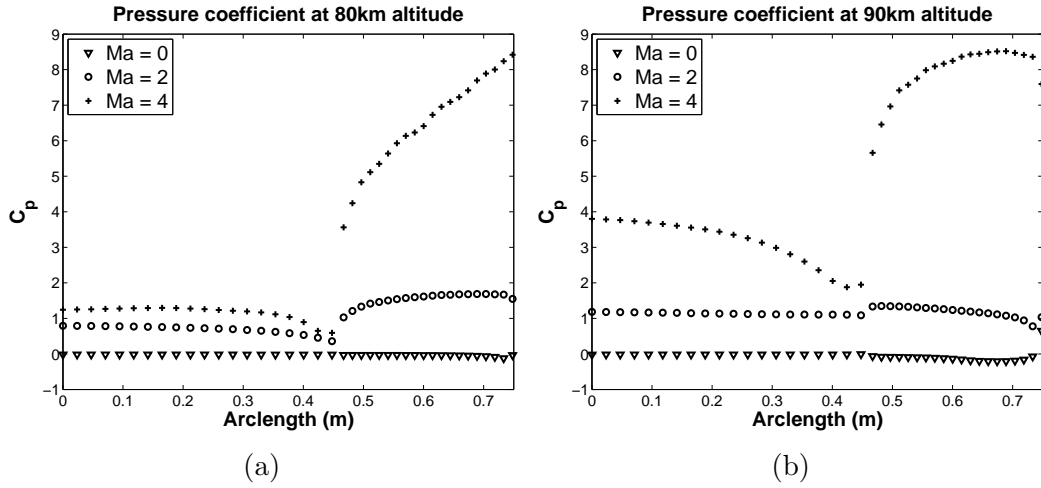


Figure 4.6: Variation of coefficient of pressure (C_p) along the arclength on critical zone 1 for (a) 80 km and (b) 90 km altitude respectively. Comparisons are made between three different Mach numbers (0, 2 and 4) for slip CFD cases.

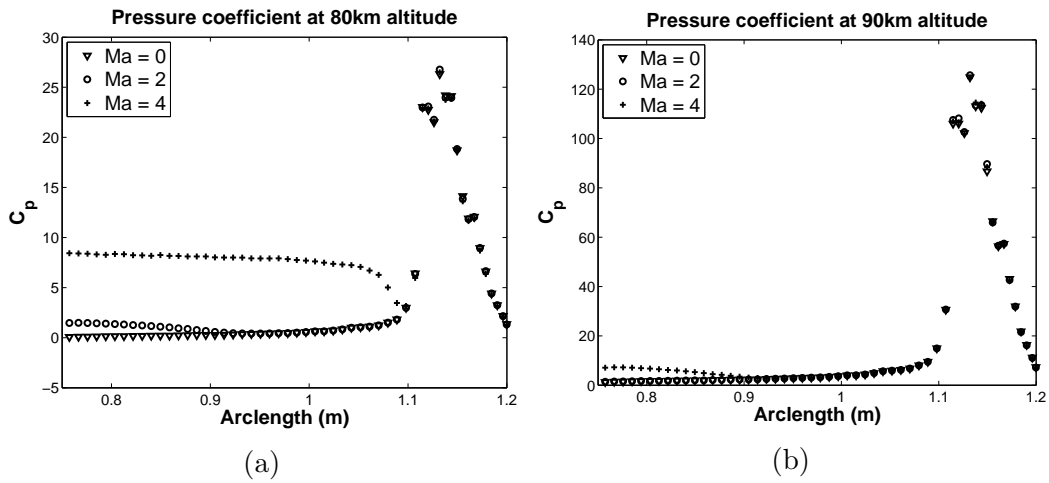


Figure 4.7: Variation of coefficient of pressure (C_p) along the arclength on critical zone 2 for (a) 80 km and (b) 90 km altitude respectively. Comparisons are made between three different Mach numbers (0, 2 and 4) for slip CFD cases.

Table 4.1: Average pressure coefficient values for different flow conditions (at 80 km and 90 km altitude, and free-stream Mach number 0, 2 and 4) and percentage deviation in between slip and no slip CFD for overall critical region.

Altitude	80km			90km		
Mach	0	2	4	0	2	4
Slip CFD	2.9963	3.7131	6.8514	14.0882	15.5066	17.0664
No-slip CFD	3.1158	3.6139	7.1236	15.2702	14.2587	16.7092
%Deviation	3.9912	2.6712	3.9731	8.3900	8.0474	2.0929

Table 4.2: Average pressure coefficient values for different flow conditions (at 80 km and 90 km altitude, and free-stream Mach number 0, 2 and 4) and percentage deviation in between slip and no slip CFD for critical zone 1.

Altitude	80km			90km		
Mach	0	2	4	0	2	4
Slip CFD	-0.0297	1.1189	3.8500	-0.0476	1.1634	5.5407
No-slip CFD	-0.0302	1.1390	3.4681	-0.0608	1.1511	5.3017
%Deviation	1.6427	1.7890	9.9193	27.8390	1.0537	4.3136

Table 4.3: Average pressure coefficient values for different flow conditions (at 80 km and 90 km altitude, and free-stream Mach number 0, 2 and 4) and percentage deviation in between slip and no slip CFD for critical zone 2.

Altitude	80km			90km		
Mach	0	2	4	0	2	4
Slip CFD	4.9175	5.3602	8.7570	23.0633	24.6133	24.3843
No-slip CFD	5.1133	5.1853	9.4445	25.0042	22.5810	23.9521
%Deviation	3.9822	3.2623	7.8511	8.4155	8.2573	1.7726

4.0.2 Coefficient of Heat Transfer

Coefficient of heat transfer C_h along a surface is a measure of net energy flux of the molecule impinging on the surface. It is defined as follows,

$$C_h = \frac{q_w}{\frac{1}{2}\rho_\infty U_\infty^3}, \quad (4.3)$$

where q_w is the heat flux on the wall and ρ_∞ , U_∞ are free-stream density and velocity respectively.

Figures 4.8 and 4.9 demonstrate the variation of coefficient of heat transfer (C_h) along the arclength on critical zone 1 and 2 respectively. Comparisons are made between different Mach numbers (0, 2 and 4) for slip CFD cases. Here, plots (a) and (b) in both figures demonstrate 80 and 90 km respectively. It can be seen in figure 4.8, that for quiescent atmosphere case, value of C_h is negative in some parts of the wall, because due to free expansion and the back flow of plumes, temperature of plumes becomes less than the wall temperature. However when free-stream flow conditions exist, recirculation zones are formed upstream of the tail of rocket, and temperature of flow increases in that region. So heat load on walls increase again and value of C_h is positive for Mach 2 and Mach 4. Table 4.4 demonstrates the variation of average C_h value with respect to altitude and free-stream Mach number throughout the critical region. It can be observed that average C_h value increases as free-stream Mach number increases. Percentage deviation in slip and noslip CFD values is reduced with the increase in free-stream Mach. It can be explained by the fact that as free-stream Mach number increases, density is higher over the critical region as particles are brought to rest from high speed in the same region. Higher density region leads to more continuume effect and less deviation in slip and no slip C_h values.

Tables 4.4, 4.5 and 4.6 demonstrate average C_h values along the arclength on entire critical zone, critical zone 1 and zone 2 respectively. It can be seen that conventional CFD is predicting higher value of C_h as compared to slip CFD. Percentage deviation in slip and no slip CFD values is more at 90 km than at 80 km for respective cases (refer table 4.4) as 90 km altitude is more deviated from continuume. Significant deviation is observed for 90 km quiescent atmosphere case (refer table 4.5 and 4.6). It indicates that conventional CFD is not able to catch degree of rarefaction as altitude increases. Also average C_h value is higher at 90 km than at 80 km altitude. It indicates that heat load increases at higher altitude as atmosphere becomes more rarified.

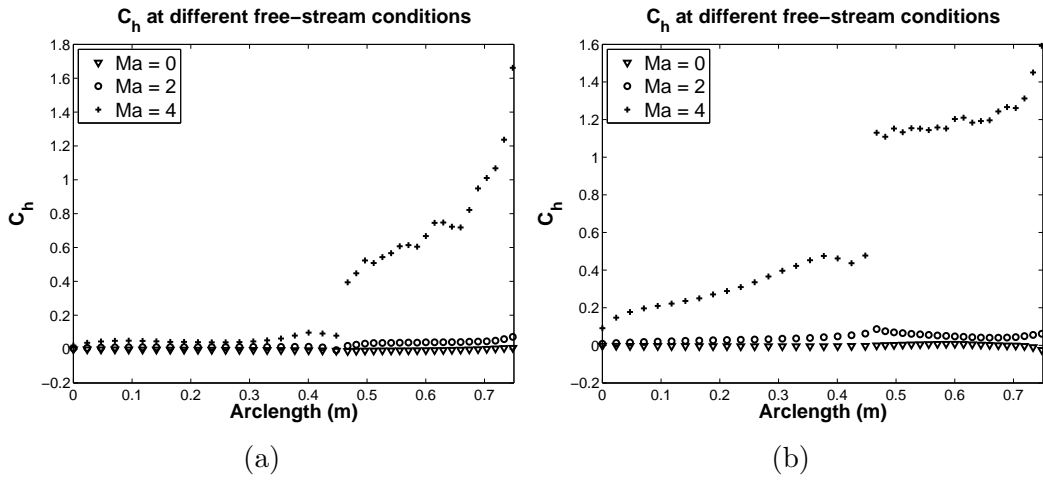


Figure 4.8: Variation of coefficient of pressure (C_h) along the arclength on critical zone 1 for (a) 80 km and (b) 90 km altitude respectively. Comparisons are made between three different Mach numbers (0, 2 and 4) for slip CFD cases.

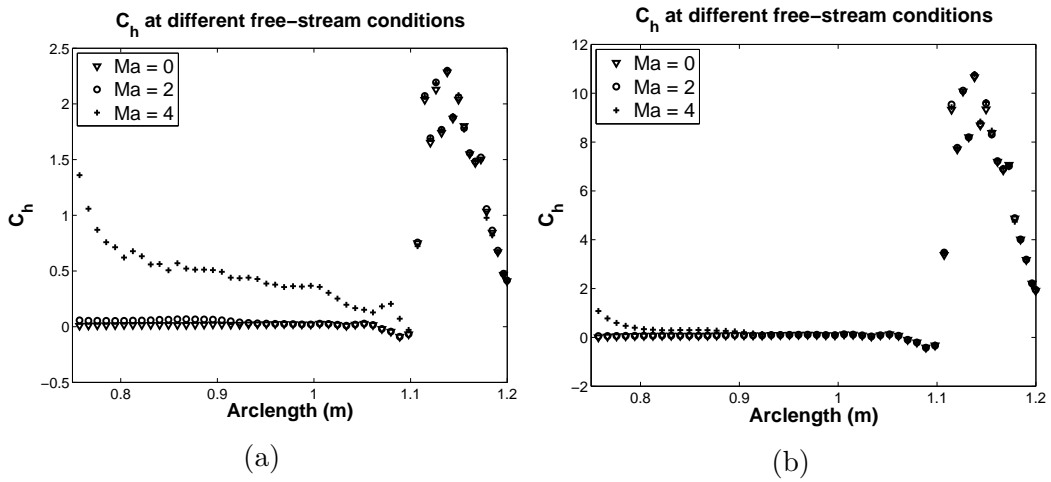


Figure 4.9: Variation of coefficient of heat transfer (C_h) along the arclength on critical zone 2 for (a) 80 km and (b) 90 km altitude respectively. Comparisons are made between three different Mach numbers (0, 2 and 4) for slip CFD cases.

Table 4.4: Average heat transfer coefficient values for different flow conditions (at 80 km and 90 km altitude, and free-stream Mach number 0, 2 and 4) and percentage deviation in between slip and no slip CFD for overall critical region.

Altitude	80km			90km		
Mach	0	2	4	0	2	4
Slip CFD	0.2157	0.2426	0.5351	0.9883	1.0547	1.3653
No-slip CFD	0.286	0.2907	0.6369	1.3305	1.2746	1.637
%Deviation	32.611	19.809	19.012	34.616	20.8465	19.901

Table 4.5: Average heat transfer coefficient values for different flow conditions (at 80 km and 90 km altitude, and free-stream Mach number 0, 2 and 4) and percentage deviation in between slip and no slip CFD for critical zone 1.

Altitude	80km			90km		
Mach	0	2	4	0	2	4
Slip CFD	-0.0044	0.0258	0.4142	-0.0014	0.0425	0.7722
No-slip CFD	-0.0037	0.0281	0.4453	0.0024	0.0496	0.8271
%Deviation	15.8946	8.6967	7.5066	71.42	16.7259	7.1110

Table 4.6: Average heat transfer coefficient values for different flow conditions (at 80 km and 90 km altitude, and free-stream Mach number 0, 2 and 4) and percentage deviation in between slip and no slip CFD for critical zone 2.

Altitude	80km			90km		
Mach	0	2	4	0	2	4
Slip CFD	0.3554	0.3802	0.6119	1.6169	1.6974	1.7419
No-slip CFD	0.4699	0.4574	0.7585	2.1731	2.0523	2.1347
%Deviation	32.2285	20.2887	23.9568	34.4037	20.9120	22.5500

4.0.3 Coefficient of Drag

Coefficient of drag along a surface is a measure of net kinetic energy flux of the molecule impinging on the surface, which is defined by

$$C_D = \frac{\text{Wall shear stress} + p}{\frac{1}{2}\rho_\infty U_\infty^2}, \quad (4.4)$$

where ρ_∞ and U_∞ are free-stream density and velocity respectively. And p is the static pressure on the wall.

Drag force consists of 2 components, which are drag due to pressure difference and drag due to friction between fluid layer and solid wall. Value of pressure is not affected with non-equilibrium effects (refer section 4.1). Therefore amount of deviation is present only due to frictional drag contribution. Significant difference between slip CFD and no-slip CFD results of C_D is observed where barrel shock is present. It indicates that C_D is sensitive to altitude variation and is affected by degree of rarefaction unlike C_p in slip flow regime. No slip CFD is predicting higher value of C_D than slip CFD as demonstrated by table 4.7.

Figures 4.10 and 4.11 show that coefficient of drag at different free-stream Mach numbers at 80 km and 90 km altitude on critical zone 1 and 2. At both 80 km (4.10a) and 90 km (4.10b) altitude, C_D values are high at 0.459 m and 0.748 m which are corners of wing (refer figure 4.3) and oblique shocks are present at these sharp corners. Coefficient of drag is not much sensitive to free-stream Mach number in near nozzle region (critical zone 2) as figure 4.11 indicates, whereas on the wall away from nozzle (critical zone 1), C_D values are higher for higher Mach number as higher the velocity, higher will be the frictional drag. C_D values are higher for 90 km altitude as compared to 80 km on critical zone 1 and reverse case is observed on critical zone 2 which is more exposed to supersonic free-stream flow than exhaust plumes. The reason being atmosphere is more rarified at 90 km leading to less number of molecules impinging on the wall and hence less frictional drag.

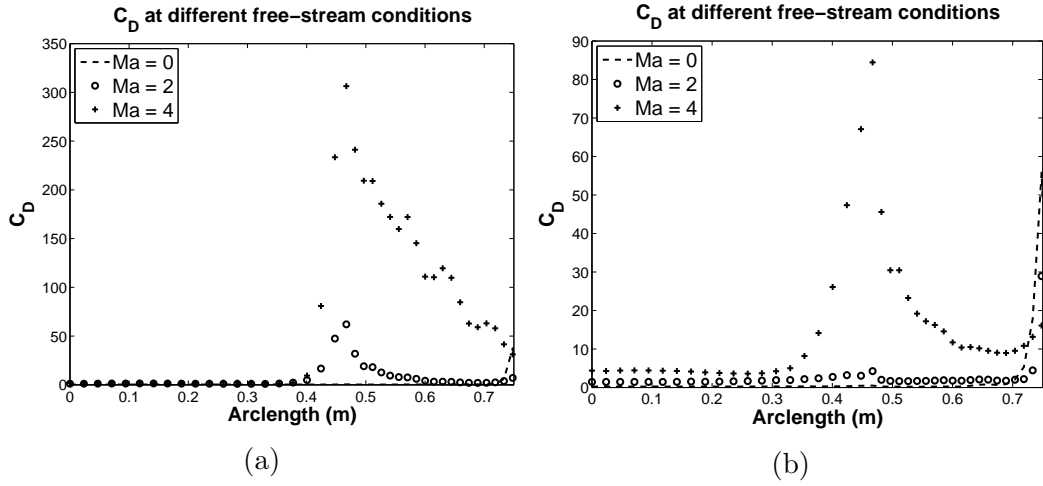


Figure 4.10: Variation of coefficient of drag (C_D) along the arclength on critical zone 1 for (a) 80 km and (b) 90 km altitude respectively. Comparisons are made between three different Mach numbers (0, 2 and 4) for slip CFD cases.

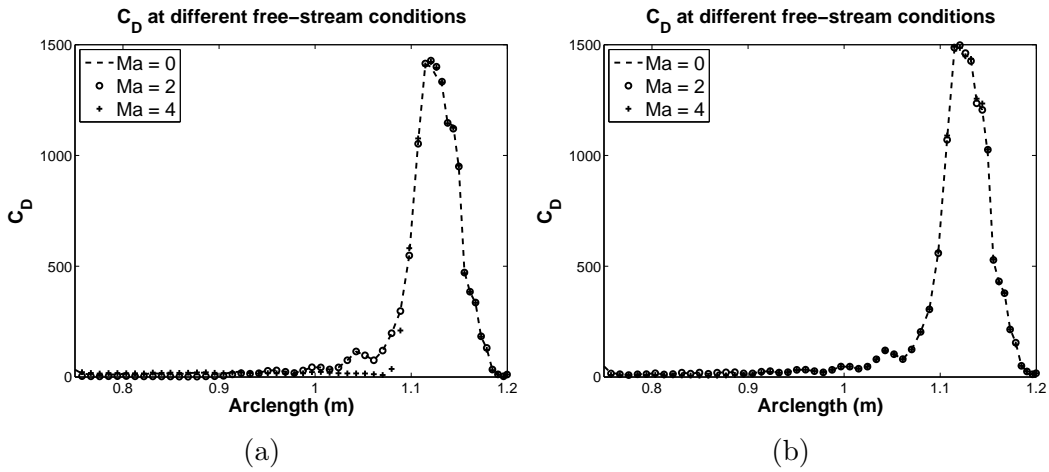


Figure 4.11: Variation of coefficient of drag (C_D) along the arclength on critical zone 2 for (a) 80 km and (b) 90 km altitude respectively. Comparisons are made between three different Mach numbers (0, 2 and 4) for slip CFD cases.

Table 4.7: Average drag coefficient values for different flow conditions and percentage deviation in slip-no slip CFD throughout the critical wall

Altitude	80km			90km		
Mach	0	2	4	0	2	4
Slip CFD	140.646	142.518	163.224	152.71	153.755	157.881
No-slip CFD	176.230	175.257	218.041	187.904	185.640	192.2206
%Deviation	25.3	22.971	33.584	23.04	20.7373	21.7503

Table 4.8: Average drag coefficient values for different flow conditions and percentage deviation in slip-no slip CFD (critical zone 1)

Altitude	80km			90km		
Mach	0	2	4	0	2	4
Slip CFD	1.5208	7.5435	75.3578	2.4401	2.7507	15.6925
No-slip CFD	1.7507	9.5342	136.4780	3.2552	3.7160	24.2487
%Deviation	15.1102	26.3895	81.1065	33.4025	35.0962	54.5248

Table 4.9: Average drag coefficient values for different flow conditions and percentage deviation in slip-no slip CFD (critical zone 2)

Altitude	80km			90km		
Mach	0	2	4	0	2	4
Slip CFD	228.9802	228.2173	219.0129	248.1205	249.6313	248.1594
No-slip CFD	287.0112	280.4783	269.8285	305.1417	301.5766	298.1131
%Deviation	25.3433	22.8997	23.2021	22.9813	20.8088	20.1297

4.0.4 Normalized density

Normalized density variation (ρ/ρ_∞) at 80 km and 90 km altitude is demonstrated in figure 4.12. Barrel shock is present at the same position i.e. 1.15 m of arclength at both the altitudes but is stronger at 90 km altitude. Normalized density is higher for higher free-stream Mach number as demonstrated in figure 4.13 because particles are brought to rest from high speed to very low speed in the same region around the critical wall.

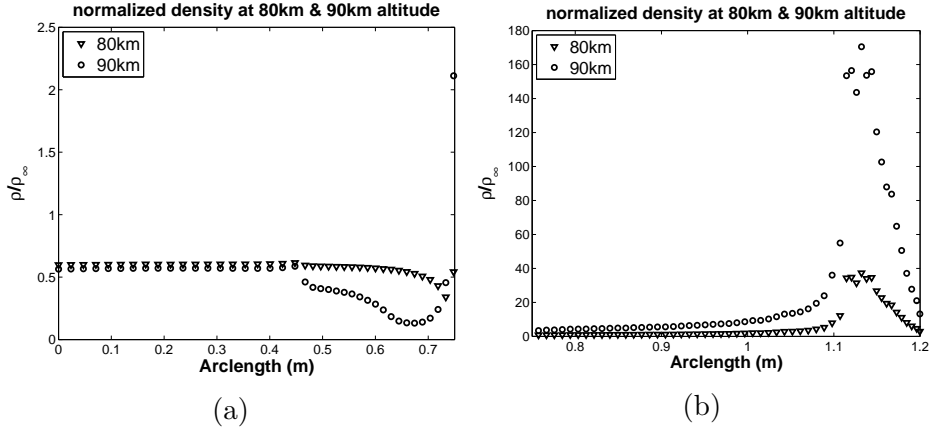


Figure 4.12: Variation of normalized density along the arclength on critical zone 1 (a) and critical zone 2 (b). Comparisons are made between 80 km and 90 km altitude conditions for quiescent atmosphere case.

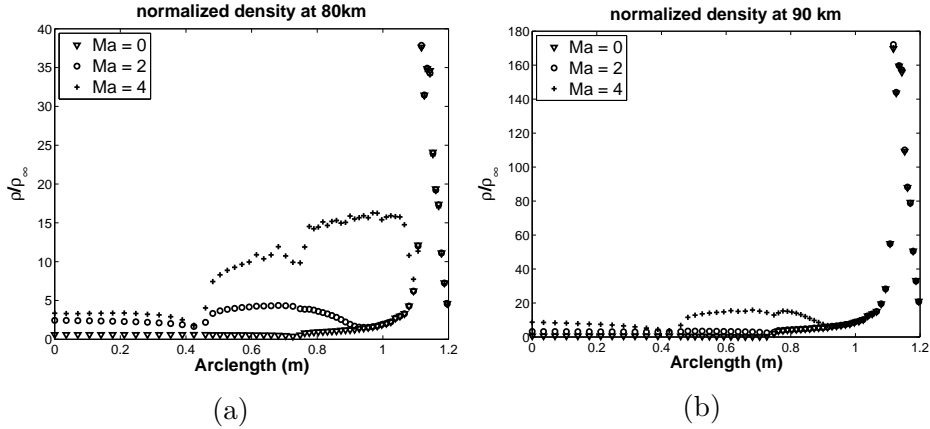


Figure 4.13: Variation of normalized density along the arclength on the entire critical zone. Comparisons are made between different free-stream Mach numbers (0, 2 and 4) at 80 km (a) and 90 km (b) altitude conditions.

4.0.5 Axial and Radial slip velocity

Normalized axial slip velocity (U_x/U_∞) and normalized radial slip velocity (U_y/U_∞) along the critical wall of rocket at 80 km and 90 km altitude are demonstrated in figure 4.14. It can be seen that backflow is more at 90 km altitude than at 80 km from axial slip velocity plot, whereas radial slip velocity is almost same at both altitudes. In figure 4.14a, axial slip is positive at 0.745 m for 80 km case and also for 90 km case, positive slip velocity is observed just before its negative values indicating back-flow. This can be explained by the phenomenon of thermal transpiration in rarefied gas flows. Due to tangential temperature gradients along the walls, the fluid starts creeping in the direction from cold towards hot adding to positive slip velocity component (see equation 1). It can be seen in figure 4.14b, radial slip is higher along the arc-length 0.75 to 1.1 m, because plumes are expanding radially away from nozzle centre-line across that region.

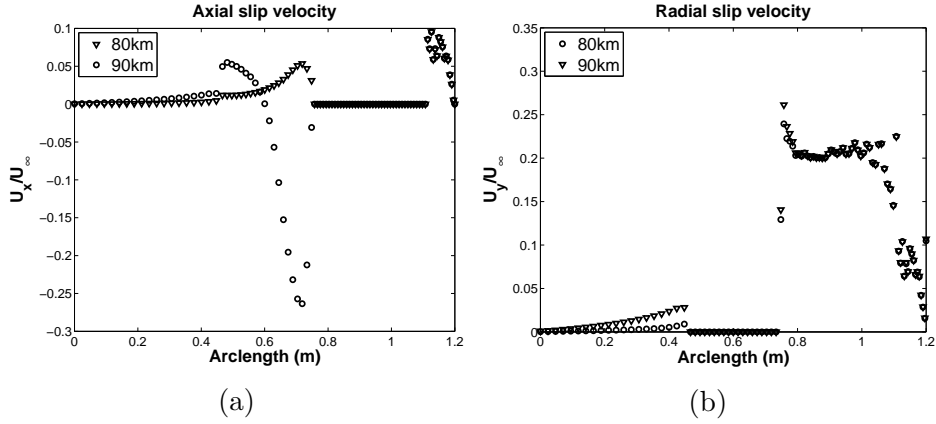


Figure 4.14: Variation of normalized axial slip velocity (a) and normalized radial slip velocity (b) along the arclength on the entire critical zone. Comparisons are made between 80 km and 90 km altitude conditions for quiescent atmosphere case.

Figure 4.15 demonstrates normalized axial slip velocity at different free-stream conditions at 80 km and 90 km altitude. In both the cases, backflow increases with increases in free-stream velocity. This is due to the fact that, recirculation zones are formed after introduction of free-stream flow.

Figure 4.16 demonstrates normalized radial velocity slip at different free-stream Mach numbers. It can be seen that radial velocity slip is not much sensitive to change in free-stream Mach number except for the critical zone 1 where free-stream flow and jet flow interact with each other. Radial slip for Mach 2 and Mach 4 case are exactly similar but slightly different from quiescent atmosphere i. e. Mach 0 case, because no free-stream and jet interaction will occur in that case.

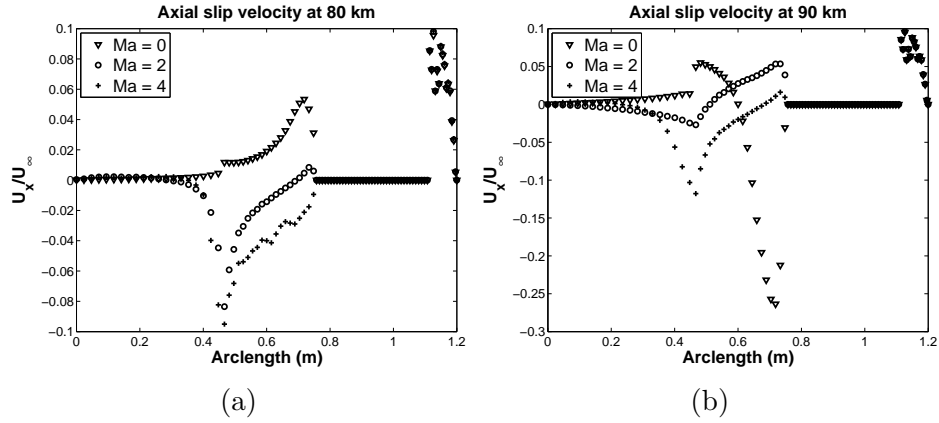


Figure 4.15: Variation of normalized axial slip velocity along the arclength on the entire critical zone. Comparisons are made between different free-stream Mach numbers (0, 2 and 4) at 80 km (a) and 90 km (b) altitude conditions.

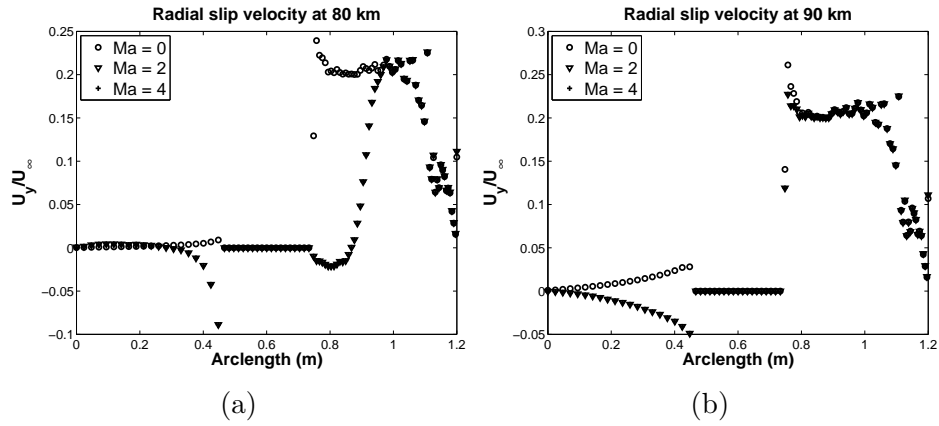


Figure 4.16: Variation of normalized radial slip velocity along the arclength on the entire critical zone. Comparisons are made between different free-stream Mach numbers (0, 2 and 4) at 80 km (a) and 90 km (b) altitude conditions.

4.0.6 Temperature Jump

Comparison of normalized temperature jump ($(T - T_w)/T_\infty$) at 80 km and 90 km altitude is demonstrated in figure 4.17. Temperature jump is higher for 90 km than at 80 km. It indicates that temperature jump is sensitive to altitude variation and it increases with the altitude. Figure 4.18 demonstrates temperature jump at 80 km and 90 km altitude for different free-stream Mach numbers. Temperature jump is sensitive to the variation in free-stream Mach number as well and increases with the increase it. It proves that non-equilibrium behaviour of energy transfer is governed by Knudsen number and Mach number.

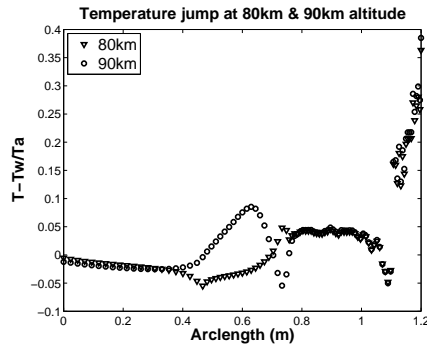


Figure 4.17: Normalised temperature jump at 80km and 90km altitude

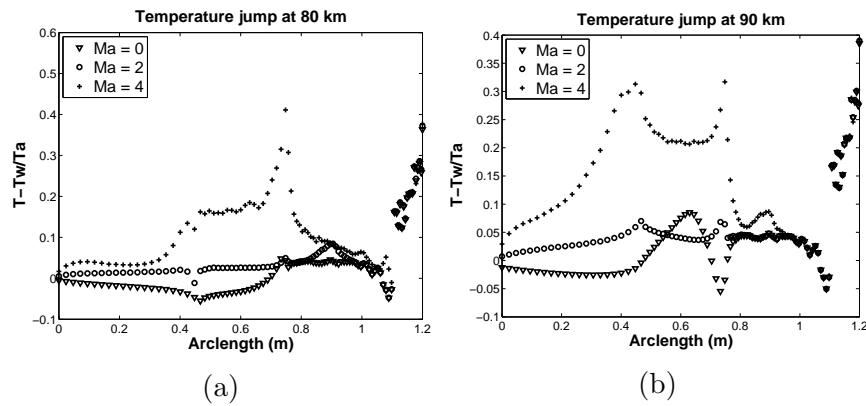


Figure 4.18: Variation of normalized temperature along the arclength on the entire critical zone. Comparisons are made between different free-stream Mach numbers (0, 2 and 4) at 80 km (a) and 90 km (b) altitude conditions.

4.0.7 Contours of different properties on the computational domain

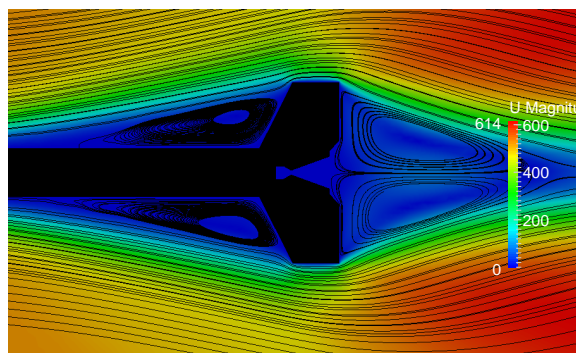


Figure 4.19: Velocity contours of free-stream flow at Mach 2 without plumes at altitude 80km

Figure 4.19 demonstrates velocity contours of freestream flow over rocket configu-

ration. Recirculation zones are formed upstream of the tail of the rocket and downstream of rocket where no jet flow is introduced. This is the steady state solution achieved for external flow problem. However when jet and free-stream both flows co-exist, boundary of inconstant pressure is developed where both flows interact.

Figure 4.20 demonstrates velocity contours at 80 km (fig a, c and e) and at 90 km (b, d and f) at free-stream Mach number 0, 2 and 4. Barrel shock which is a typical characteristic of under-expanded jets is the line of demarcation between interior region and outer region, where the former is independent of ambient pressure and the later is influenced by the ambient pressure [46], can be seen in the contours. Looking at the interior volume of the barrel shock, a large expansion fan is present with its boundaries defined by a recompression shock. For quiescent atmosphere case (Fig 4.20a and 4.20b), more back-flow at 90 km altitude is observed as barrel shock is clearly shifted backwards which supports the fact that rarefaction leads to stonger shock and higher backflow. For free-stream Mach 2 case, vortices are formed upstream of the jet flow because the barrel shock acts as a blunt body obstruction to the incoming flow. When freestream Mach is increased further, i.e. for freestream Mach 4 case, two counter-rotating separating vortices are observed upstream of wings (See Fig 4.20e and 4.20f). It is observed that jet flow is more deflected towards centreline at higher Mach number and length of recirculation zone increases with the increase in Mach number and altitude.

Figure 4.21 demonstrates temperature contours at 80 km (fig a, c and e) and at 90 km (b, d and f) at free-stream Mach number 0, 2 and 4. Jet flow expands freely at higher altitudes and it expands to the extent that the pressure of jet flow drops even below the ambient pressure and consequently the temperature of the jet flow. When free-stream Mach increases, high temperature zones are formed upstream of barrel shock due to collision of free-stream flow with jet flow, and impingement shock wave at their interaction and oblique shocks at the corners of the wing of rocket.

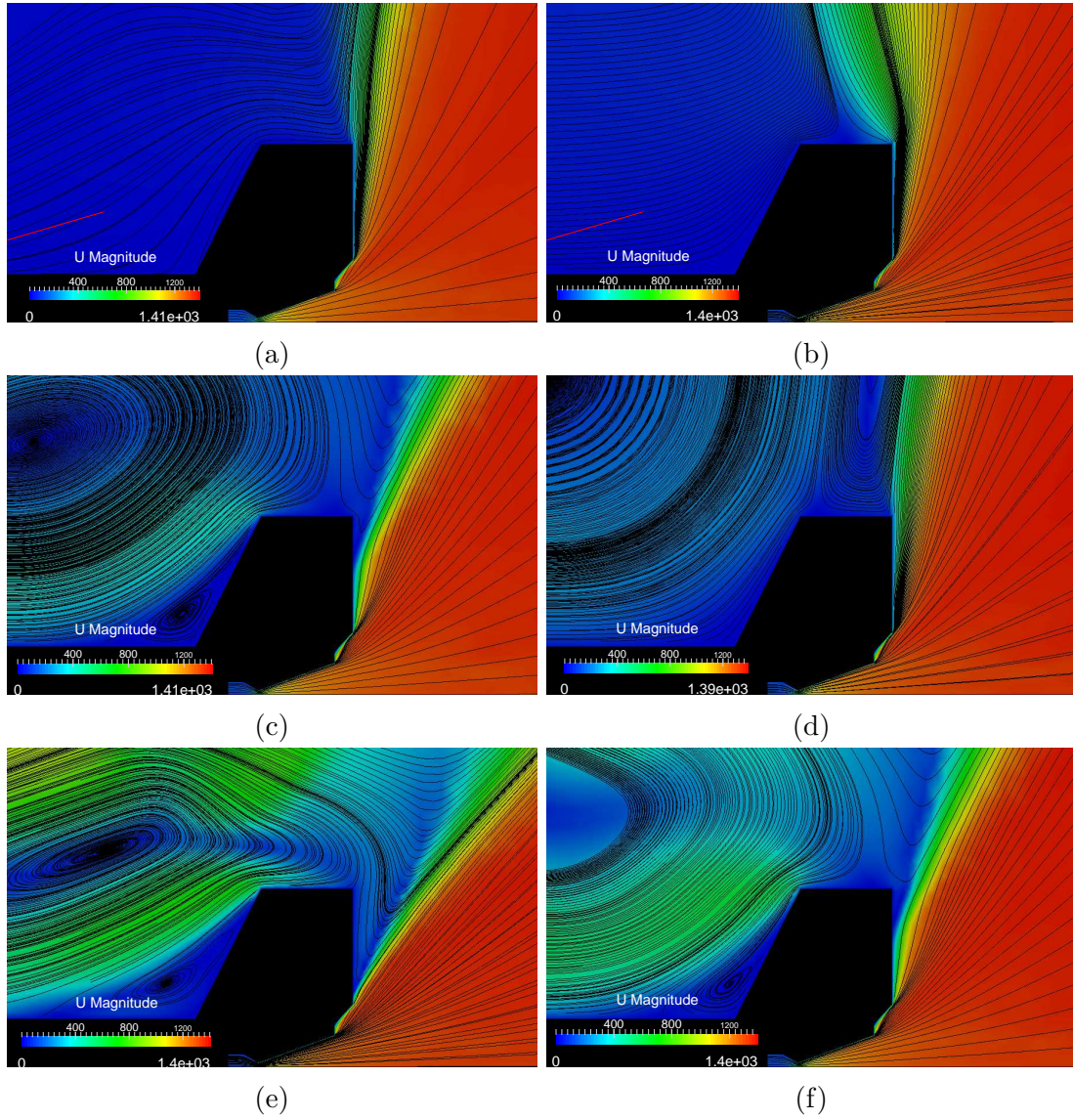


Figure 4.20: Velocity contours at 80km altitude for quiscent atmosphere case (a), freestream Mach 2 case (c), freestream Mach 4 case (e). Velocity contours at 90km altitude for quiscent atmosphere case (b), freestream Mach 2 case (d), freestream Mach 4 case (f). Results of slip CFD are reported.

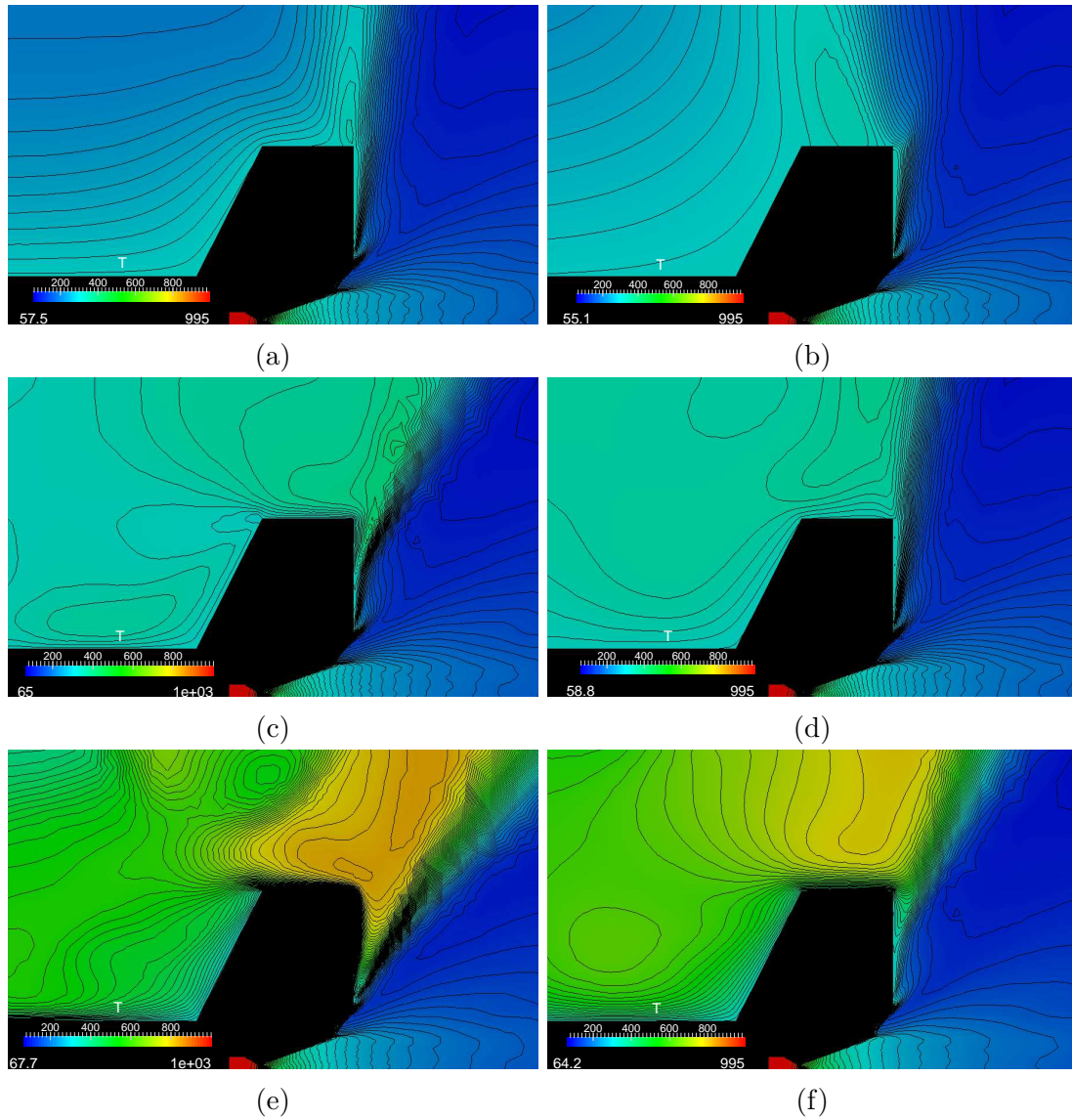


Figure 4.21: Temperature contours at 80km altitude for quiescent atmosphere case (a), freestream Mach 2 case (c), freestream Mach 4 case (e). Temperature contours at 90km altitude for quiescent atmosphere case (b), freestream Mach 2 case (d), freestream Mach 4 case (f). Results of slip CFD are reported.

Chapter 5

Conclusion and Future work

We have presented aero-thermodynamic parameters on the critical region of rocket configuration where non-equilibrium phenomenon of plume expansion and backflow, and interaction with supersonic free-stream cross-flow occurs at high altitudes of 80 km and 90 km. The *rhoCentralFoam* solver is validated against experimental data for nozzle flow expanding in vacuum and external flow over rocket at 5 km altitude conditions. We have carried out detailed investigations to report the non-equilibrium effects on the drag, pressure and heat transfer coefficients resulting because of plume impingement on the critical region of wall by comparing the conventional CFD results with the slip CFD results.

Coefficient of pressure is not much sensitive to change in altitude and to change in freestream Mach number on the critical region under study. However heat transfer coefficient and drag coefficient on critical zone 1 are significantly sensitive to altitude variation as well as change in free-stream Mach number. It is observed that no slip CFD predicts higher values of C_h and C_D than slip CFD, which may lead to over-design of the critical zone. Percentage deviation in no slip and slip CFD results is more pronounced with the increase in free-stream Mach number and at higher altitude. It is evident from heat transfer coefficient values that non-equilibrium description of energy transfer depends on both the Knudsen number and Mach number.

Hence, the accuracy of theoretical/continuum models for exhaust plumes back flow analysis in the slip and transition flow regions cannot be decided based upon the mere comparisons for pressure coefficients, which are usually reported by experiments. Heat/energy transfer plays key role in determining the deficiencies in the classical continuum methods for high-speed rarefied gas flows.

The first-order non-equilibrium boundary conditions are not sufficient to accurately describe the non-equilibrium gas flow physics. We may need to incorporate

both the higher order boundary conditions as well as the non-linear constitutive relations into the Navier-Stokes equations framework to report better predictions. This can be done as a future work to this current work. This is very important from the numerical simulations perspective as particle methods are still computationally intensive for simple gas flows and indeed expensive for 3-D complex geometries.

References

- [1] E. Bigarella, J. L. F. Azevedo, and O. Mello. Normal force calculations for rocket-like configurations. *Journal of the Brazilian Society of Mechanical Sciences and Engineering* 26, (2004) 290–296.
- [2] D. E. Rothe. Electron-beam studies of viscous flow in supersonic nozzles. *AIAA Journal* 9, (1971) 804–811.
- [3] C. Glass. A parametric study of jet interactions with rarefied flow. In International symposium on rarefied gas dynamics. 1999 .
- [4] G. Dettleff and M. Grabe. Basics of Plume Impingement Analysis for Small Chemical and Cold Gas Thrusters. Technical Report, DTIC Document 2011.
- [5] E. S. Love and C. E. Grigsby. Some studies of axisymmetric free jets exhausting from sonic and supersonic nozzles into still air and into supersonic streams .
- [6] E. S. Love. An approximation of the boundary of a supersonic axisymmetric jet exhausting into a supersonic stream. *Journal of the Aerospace Sciences* 25, (1958) 130–131.
- [7] T. C. Adamson and J. A. Nicholls. On the structure of jets from highly under-expanded nozzles into still air: final report .
- [8] E. Latvala. Spreading of rocket exhaust jets at high altitudes. *ASTIA Document No. AD-215866, AEDC-TR-59-11 (June 1959)* .
- [9] M. Woronowicz. Initial molecular flow observations on bipolar planetary nebulae gaskinetics. *AIAA Paper* 599.
- [10] F. P. Boynton. Exhaust plumes from nozzles with wall boundary layers. *Journal of Spacecraft and Rockets* 5, (1968) 1143–1147.

- [11] G. A. Simons. Effect of nozzle boundary layers on rocket exhaust plumes. *AIAA journal* 10, (1972) 1534–1535.
- [12] C. Cai, Q. Sun, and A. Vanderwyst. Analytical exact solutions for unsteady collisionless plume flows in a vacuum. *Acta Astronautica* 91, (2013) 218–227.
- [13] D. Manski and G. Hagemann. Influence of rocket design parameters on engine nozzle efficiencies. *Journal of propulsion and power* 12, (1996) 41–47.
- [14] P. Bakker, W. Bannink, P. Servel, and P. Reijasse. CFD validation for base flows with and without plume interaction. Technical Report, DTIC Document 2006.
- [15] B. Buanga, V. Hannemann, H. Ludeke, A. Mack, and Y. You. Modeling of the interaction between a space vehicles external flow and its plume .
- [16] V. Viti, R. Neel, and J. A. Schetz. Detailed flow physics of the supersonic jet interaction flow field. *Physics of Fluids (1994-present)* 21, (2009) 046,101.
- [17] Z. Rana, B. Thornber, and D. Drikakis. Transverse jet injection into a supersonic turbulent cross-flow. *Physics of Fluids (1994-present)* 23, (2011) 046,103.
- [18] J. M. Burt and I. D. Boyd. High altitude plume simulations for a solid propellant rocket. *AIAA journal* 45, (2007) 2872–2884.
- [19] S. Gimelshein, A. Alexeenko, and D. Levin. Modeling of the interaction of a side jet with a rarefied atmosphere. *Journal of spacecraft and rockets* 39, (2002) 168–176.
- [20] F. E. Lumpkin. A CFD/DSMC analysis of plumes and plume impingement during Shuttle/Mir docking. In AIAA, Thermophysics Conference, 30 th, San Diego, CA. 1995 .
- [21] J. Papp, R. Wilmoth, C. Chartrand, and S. Dash. Simulation of high-altitude plume flow fields using a hybrid continuum CFD/DSMC approach. In Paper No. AIAA-2006-4412, 42nd AIAA/ASME/SAE/ASEE Joint Propulsion Conference & Exhibit. 2006 9–12.
- [22] B. He, J. Zhang, and G. Cai. Research on vacuum plume and its effects. *Chinese Journal of Aeronautics* 26, (2013) 27–36.

- [23] S. F. Gimelshein, A. A. Alexeenko, D. C. Wadsworth, and N. E. Gimelshein. The influence of particulates on thruster plume/shock layer interaction at high altitudes. *AIAA Paper 766*, (2005) 2005.
- [24] P. Vashchenkov, A. Kudryavtsev, D. Khotyanovsky, and M. Ivanov. DSMC and Navier-Stokes study of backflow for nozzle plumes expanding into vacuum. Technical Report, DTIC Document 2005.
- [25] A. Kurganov and E. Tadmor. New high-resolution central schemes for nonlinear conservation laws and convection–diffusion equations. *Journal of Computational Physics* 160, (2000) 241–282.
- [26] A. Kurganov, S. Noelle, and G. Petrova. Semidiscrete central-upwind schemes for hyperbolic conservation laws and Hamilton–Jacobi equations. *SIAM Journal on Scientific Computing* 23, (2001) 707–740.
- [27] C. J. Greenshields, H. G. Weller, L. Gasparini, and J. M. Reese. Implementation of semi-discrete, non-staggered central schemes in a colocated, polyhedral, finite volume framework, for high-speed viscous flows. *International journal for numerical methods in fluids* 63, (2010) 1–21.
- [28] R. Ladenburg, C. Van Voorhis, and J. Winckler. Interferometric studies of faster than sound phenomena. Part II. Analysis of supersonic air jets. *Physical Review* 76, (1949) 662.
- [29] A. Bansal, A. Feldick, and M. Modest. Simulation of Hypersonic Flow and Radiation over a Mars Reentry Vehicle Using OpenFOAM. In 50th AIAA Aerospace Sciences Meeting including the New Horizons Forum and Aerospace Exposition. 2012 .
- [30] S. Nakao, M. Kashitani, T. Miyaguni, and Y. Yamaguchi. A study on high subsonic airfoil flows in relatively high Reynolds number by using OpenFOAM. *Journal of Thermal Science* 23, (2014) 133–137.
- [31] W. S. Hinman, C. T. Johansen, C. J. Arisman, and W. C. Galuppo. Numerical Investigation of Laminar near Wake Separation on Circular Cylinders at Supersonic Velocities .
- [32] R. K. Soni, N. Arya, and A. De. Computation of Supersonic Flow Past Backward Facing Step in OpenFOAM. In Book of Abstracts. Department of Aerospace Engineering, IIT Kanpur, 2014 22.

- [33] E. B. Arkilic, M. A. Schmidt, and K. S. Breuer. Gaseous slip flow in long microchannels. *Microelectromechanical Systems, Journal of* 6, (1997) 167–178.
- [34] S. Colin. Rarefaction and compressibility effects on steady and transient gas flows in microchannels. *Microfluidics and Nanofluidics* 1, (2005) 268–279.
- [35] M. Gad-el Hak. The fluid mechanics of microdevices the Freeman scholar lecture. *Journal of Fluids Engineering* 121, (1999) 5–33.
- [36] G. Bird. Molecular gas dynamics and the direct simulation monte carlo of gas flows. *Clarendon, Oxford* 508.
- [37] E. Van der Weide, H. Deconinck, E. Houtman, and P. Bakker. Computational Analysis of Base Flow/Jet Plume Interaction. In *Aerothermodynamics for space vehicles*, volume 426. 1999 605.
- [38] E. M. Tridas. Experimental and Numerical Investigation of an Electrospray RF Ion Funnel .
- [39] P. Freitas. Numerical Simulation of Compressible Flow Over a Deep Cavity .
- [40] F. R. Menter. Zonal two equation k-turbulence models for aerodynamic flows. *AIAA paper* 2906, (1993) 1993.
- [41] F. Menter, M. Kuntz, and R. Langtry. Ten years of industrial experience with the SST turbulence model. *Turbulence, heat and mass transfer* 4.
- [42] L. Davidson. Fluid mechanics, turbulent flow and turbulence modeling. *Chalmers University of Technology, Goteborg, Sweden (Nov 2011)* .
- [43] P. Biju Kuttan and M. Sajesh. Optimization of Divergent Angle of a Rocket Engine Nozzle Using Computational Fluid Dynamics. *Optimization* 2, (2013) 196–207.
- [44] E. Arlemark, G. Markelov, and S. Nedeaa. Rebuilding of Rothe’s nozzle measurements with OpenFOAM software. In *Journal of Physics: Conference Series*, volume 362. IOP Publishing, 2012 012040.
- [45] M. Ivanov, G. Markelov, A. Ketsdever, and D. Wadsworth. Numerical study of cold gas micronozzle flows. American Institute of Aeronautics and Astronautics, 1999.

- [46] M. Schoones and W. Bannink. Base flow and exhaust plume interaction. Part 1: Experimental study .